



Fraunhofer Institut
Kurzzeitdynamik
Ernst-Mach-Institut

Characterization of the Material Microstructure for Reactive Material Design

3rd Quarterly Progress Report II/2008

Report I-32/08

Prepared by:
Arno Klomfass

Contributions:
Frank Bagusat
Sascha Knell
Konrad Linnemann
Martin Sauer
Martin Steinhauser

Management:
Arno Klomfass

August 2008
Freiburg, Germany

Report Documentation Page				Form Approved OMB No. 0704-0188	
Public reporting burden for the collection of information is estimated to average 1 hour per response, including the time for reviewing instructions, searching existing data sources, gathering and maintaining the data needed, and completing and reviewing the collection of information. Send comments regarding this burden estimate or any other aspect of this collection of information, including suggestions for reducing this burden, to Washington Headquarters Services, Directorate for Information Operations and Reports, 1215 Jefferson Davis Highway, Suite 1204, Arlington VA 22202-4302. Respondents should be aware that notwithstanding any other provision of law, no person shall be subject to a penalty for failing to comply with a collection of information if it does not display a currently valid OMB control number.					
1. REPORT DATE 01 AUG 2008		2. REPORT TYPE N/A		3. DATES COVERED	
4. TITLE AND SUBTITLE Characterization of the Material Microstructure for Reactive Material Design 3rd Quarterly Progress Report II/2008				5a. CONTRACT NUMBER	
				5b. GRANT NUMBER	
				5c. PROGRAM ELEMENT NUMBER	
6. AUTHOR(S)				5d. PROJECT NUMBER	
				5e. TASK NUMBER	
				5f. WORK UNIT NUMBER	
7. PERFORMING ORGANIZATION NAME(S) AND ADDRESS(ES) Fraunhofer Freiburg, Germany				8. PERFORMING ORGANIZATION REPORT NUMBER	
9. SPONSORING/MONITORING AGENCY NAME(S) AND ADDRESS(ES)				10. SPONSOR/MONITOR'S ACRONYM(S)	
				11. SPONSOR/MONITOR'S REPORT NUMBER(S)	
12. DISTRIBUTION/AVAILABILITY STATEMENT Approved for public release, distribution unlimited.					
13. SUPPLEMENTARY NOTES					
14. ABSTRACT					
15. SUBJECT TERMS					
16. SECURITY CLASSIFICATION OF:			17. LIMITATION OF ABSTRACT UU	18. NUMBER OF PAGES 81	19a. NAME OF RESPONSIBLE PERSON
a. REPORT unclassified	b. ABSTRACT unclassified	c. THIS PAGE unclassified			

Characterization of the Material Microstructure for Reactive Material Design

3rd Quarterly Progress Report II/2008

Report I-32/08

Ordering Customer:	Office of Naval Research
Project Number	006 276 480
Contract Number:	Award No. N00014-07-1-1053
Classification:	Restricted Distribution

**Prepared by/
Management:**

A. Klomfass
Principal Investigator,
Head of Department – Numerical Simulation

Prof. Dr. K. Thoma
Director of Ernst-Mach-Institut

Table of Contents

1	General Overview	4
2	Overview on Current Work	6
2.1	Material Acquisition and Testing (Tasks 3.1, 3.2)	6
2.2	Structure Generator (Task 1)	6
2.3	Advanced Methods for FE Solvers (Task 2.2)	8
2.4	Simulation of Tests (Task 3.3)	9
3	Material Testing	10
3.1	Introduction and Material Delivery Status	10
3.2	Overview over Experimental Techniques	11
3.3	Results of Tensile Tests	12
3.4	Results of Planar Plate Tests	18
3.5	Results of Inverse Taylor Tests	31
3.6	Conclusions and Consequences for Future Tests	35
4	Structure Generator	37
4.1	Features and Statistics of the Investigated Micrographs	37
4.2	General Remarks on Structure Models	42
4.3	Technical and Algorithmic Details of POLYGRAIN	43
4.4	Further Developments of POLYGRAIN	46
4.5	Development of a Voxel Based Method	49
4.6	Application of GEODICT	51
4.7	Application of SIMPLEWARE	54
4.8	Next Steps	56
5	Advanced Methods for FE Solvers	57
5.1	Status of MESOFEM	57
5.2	Accomplished Tasks	58
5.3	Next Steps	66
6	Alternative Methods and Simulation of Tests	67
6.1	Requirements and Approach for the Simulation	67
6.2	Direct Simulation with Hexahedral Meshes	68
6.3	Preliminary Assessment	75
7	References	77

1 General Overview

The aim envisaged in this project is the development and validation of numerical methods for the mechanical simulation of materials at grain scale. These methods shall enable predictive analysis of the dependencies of the mechanical properties – especially the fragmentation behavior – on the morphological and constitutive nature of a material at grain scale. Simulation capability of this kind can be effectively applied to design new materials with specially tailored mechanical properties.

Specifically, this project is motivated by the aim to design (metallic) materials, which fragment under certain dynamic loading conditions into small particles, which can chemically react with a suitable ambient medium, such as shock heated ambient air or hot detonation products. Such materials could be effectively used to devise new or improved weapons with enhanced mechanical and/or thermal effects.

The desired numerical simulation capability comprises two parts. First, a method for the numerical generation of realistic microstructures must be developed. From these microstructures, computational grids are generated within a representative volume element of a material using readily available meshing methods. Second, a finite-element based solver for the time dependent continuum mechanical conservation equations must be developed, which permits a three-dimensional, time dependent simulation of the response of the representative volume element to applied external loads, including a treatment of inter-grain failure and fragmentation. Both such methods are not available on the commercial software market; neither is there any satisfactory and persistent treatment known in the scientific literature yet. Within the project existing, suitable methods will be adapted and further developed towards the required capabilities.

In addition, experimental investigations will be conducted aiming at the validation of the methods and models. These experiments will consist of standard material characterization tests, microstructural analysis and specifically selected fragmentation tests. The tests and analysis will be applied to two different base materials and a mixture of those materials. The selection of suitable materials for these validation tests is also a part of this project.

Upon completion of the methods and their validation, the application of the methods will be demonstrated within a simulation based process, where the

fragmentation characteristics of the mixture material are improved by altering mixture and morphological parameters.

The project is subdivided into the following working packages:

Task 1: Structure Generator

- 1.1 Generalization for multi-material porous microstructures
- 1.2 Optimization of meshing

Task 2: Advanced Methods for Microstructural FE Solvers

- 2.1 Constitutive models
- 2.2 Appropriate interface and element formulations
- 2.3 Code performance
- 2.4 Code verification

Task 3: Material Analysis and Validation of Numerical Methods

- 3.1 Selection and procurement of materials
- 3.2 Material testing and microstructural analysis
- 3.3 Simulation of tests, evaluations and model improvements

Task 4: Virtual Material Design Process

- 4.1 Virtual improvement of fragmentation properties
- 4.2 Fragmentation tests on improved microstructures

Reporting on the work progress will be through quarterly status reports. Full technical reports will be issued instead of quarterly status reports upon completion of tasks 1 to 4, respectively.

This is the third quarterly status report. The following chapters will describe the status and progress of work in **the tasks 1, 2.2 and 3**. The next status report is planned for October 2008.

2 Overview on Current Work

2.1 Material Acquisition and Testing (Tasks 3.1, 3.2)

It was previously decided (cf. 2nd quarterly status report, [1]) that the materials to be used in this project are compressed and slightly sintered powders of pure Fe, pure Cu and a mixture of both.

Initial tests were conducted with a few samples of these materials, which indicated their appropriateness for the purposes of this project, [1]. Meanwhile a larger quantity of materials was manufactured and delivered by Fraunhofer Institute IFAM. The remaining lot of materials will be delivered in August/September.

The tests conducted by now were quasi-static tensile tests, high-velocity flyer-plate impact tests and inverse Taylor tests at different conditions.

Details on the applied testing methods and results obtained are found in chapter 3. The presented results also include high-speed visualizations of spallation and fragmentation processes. Videos are provided on a CD, which is included in this report. As the report is partially distributed as PDF only, the videos will be made available for downloading for the recipients of the report.

2.2 Structure Generator (Task 1)

The capability to generate geometric models of grain distributions in a controllable way is an important part of the overall aims of this project:

- (1) For the validation of numerical models and methods, it is required to produce virtual copies of real material samples, which are tested in experiments.
- (2) For improved understanding of structure-property relations and for the design of new materials, it is desired to generate generic grain distributions in terms of statistic parameters.

Regarding the first issue, there are two basic choices. First, **true virtual copies of real material samples** can be considered. This obviously requires 3-D information of the grain distribution in the real material. Such can in principle be obtained by computer tomography (CT). A discrete distribution is in this case rendered on an equidistant, orthogonal, finite-volume grid, also called voxel

grid (voxel: the three-dimensional pendant to the pixel). From experience it is known, that this works well on porous materials. However, grain boundaries between grains of identical or similar material are typically not recognizable in CT data. True copies of the materials considered in this project are thus hard to achieve.

Alternatively, **virtual copies of a real material sample in terms of statistics of the microstructure** can be considered. To obtain the relevant statistics of grain sizes and shapes, a few or even a single 2-D micrograph can be used. The distribution of the selected parameters can be extracted from the micrographs either by means of image processing software or through measuring by hand. Fully automated image processing is not trivial, as different material constituents and pores must be distinguished. This is important as each constituent and the pores can possess their own statistics.

Once the statistical distributions are determined, a **structure generator** must be used to create the geometrical model of the grain distribution. Depending on the type of structure generator, different processes are possible:

- The structure generator POLYGRAIN developed by EMI delivers a set of interconnected grain boundaries defined through sets of grain edges and corner points. This geometry model can be used to obtain a tetrahedral mesh through readily available mesh generators like TETGEN, [2].
- Other structure generators create a voxel based distribution of material constituents. Such geometry models thus have step-shaped grain boundaries (if the orientation is not parallel to a grid plane). Such data can either directly be used for simulations based on hexahedral grids. If smooth grain boundaries are desired, a further processing of the raw voxel data is required, which again renders a mesh of tetrahedral elements.

In addition to our work on POLYGRAIN, we are exploring the performance of structure generators of the second type, which create voxel based material distributions. A generator of this kind has recently been developed at EMI. Another voxel based generator is implemented in GEODICT. This software was developed by the Fraunhofer Institute ITWM, [3]. The ability to convert such voxel based material distributions into grain distributions with smooth grain boundaries defined on tetrahedral meshes is offered by the software SIMPLEWARE, [4].

As a test candidate for all these options, we chose a FeCu material. For this material we determined the statistical distributions of grain sizes and shapes and generated geometric models and meshes. Chapter 4 gives further details about this work and results obtained so far.

2.3 Advanced Methods for FE Solvers (Task 2.2)

An explicit FE solver, which works with tetrahedral elements for the grains and interface elements for the grain boundaries, is considered the best choice for the numerical simulation of a material on the grain level. The tetrahedral elements permit a flexible modeling of arbitrary grain shapes and distributions, while the interface elements enable a physically based modeling of failure at grain boundaries. Besides tetrahedral elements and interface elements, a third important issue for such a solver is a contact algorithm, which efficiently handles the multiple internal contacts, which occur upon failure under shear or compression. A solver of this type is being developed in this project under the name MESOFEM.

The majority of work on MESOFEM was dedicated to the conception of a tetrahedral element, which works efficiently and accurately with explicit time integration for elastic and particularly for plastic deformations. While tetrahedral elements are readily implemented for pure elastic (isotropic and orthotropic) deformations, no suitable formulation for plastic deformations could be found in the literature yet. While the conception of the desired element is still under way, the implementation of interface elements has recently been achieved.

Further details on the current work on tetrahedral elements and interface elements are given in chapter 5.

In addition to the work on MESOFEM, the exploration of two alternative approaches was begun. These are:

- LS-DYNA simulation of grain agglomerates in a representative volume element modeled with hexahedral elements. In the approach followed here, the grain boundaries are modeled as layers with finite thickness of at least one grid cell. This is a simplistic but very flexible approach.
- MD-Cube simulation of grain agglomerates in a representative volume element modeled with densely packed particles. Here, the grain boundaries are modeled through a modified particle potential that is applied between particles of different grains.

The motivation for the additional investigations is twofold. Firstly, the generation of virtual material samples is comparatively simple and flexible if the material distributions are rendered on hexahedral (voxel-)grids. In fact, such models can directly be created by structure generators like GEODICT, cf. chapter 2.2. Secondly, we aim to provide an applicable simulation method in due time, while the working on the tetrahedral element for MESOFEM continues.

A voxel based model of a Cu sample was used as test subject for the above mentioned approaches. Details about the LS-DYNA simulations and the results obtained are found in chapter 6. The approach with MD-Cube will be reported in a subsequent report.

2.4 Simulation of Tests (Task 3.3)

Initial simulations for the Cu sample have been carried out with LS-DYNA using the approach described above. A physical model has been set up and calibrated to the results of the tensile tests. This model has then been used for investigations of the material response to dynamic loading. Results of these simulations are included in chapter 6.

3 Material Testing

3.1 Introduction and Material Delivery Status

Basic requirements for the copper (Cu) and iron (Fe) powders that are used as reference materials were described in the last two quarterly reports.

The material tests described in the last quarterly report were conducted with samples, which were only cold pressed or cold pressed and subsequently sintered at different temperatures. Because a pure cold pressing process is not sufficient to generate the needed stability, sintering temperatures between 600 °C and 800 °C were tested. As a result of these previous experiments, we have chosen a sintering temperature of 700 °C for the second and last (third) lot of materials. This temperature delivers good mechanical stability.

The major part of the second lot was meanwhile produced and delivered by Fraunhofer IFAM:

- Plates of sintered Fe powder processed at two different pressures of 400 MPa and 580 MPa.
- Plates of sintered Cu powder processed at a pressure of 400 MPa.
- Plates of a mixture of 50 % Cu powder and 50 % Fe powder processed at a pressure of 400 MPa.

Plates of the Cu and CuFe mixture pressed at a pressure of 580 MPa were not available until the end of July 2008.

Compared with the material tested in the last report, the process of preparation was different in the following way. The previous materials were produced in a small press so that only one sample was generated in one process step. The current lot was created with a large press, which produced plates in the format of 130 mm x 130 mm with a thickness of 8 mm.

The two manufacturing pressures of 400 MPa and 580 MPa generate different porosities of the materials. These porosities are summarized in table 3.1.

From the delivered plates our testing samples were manufactured in our workshop with a wire spark erosion machine.

Table 3.1: Porosities of the material from the current lot. The porosity is derived by the geometric size of the samples and their masses. IFAM data are based on the raw plates (no perfect squares). We used the Taylor nails and the planar impact samples.

	Pressure MPa	Porosity % (IFAM estimation)	Porosity % derived from our samples
Fe	400	15.1	12.1–15.1
Fe	580	9.8	10.7–11.3
Cu	400	10.1	8.8–10.1
CuFe	400	15.8	11.6–14.1

3.2 Overview over Experimental Techniques

Due to the slightly modified production technique, the mechanical properties of the materials were expected to differ from those of the first lot. Therefore, basic tensile tests were carried out again under the same experimental conditions as for the samples from the first lot.

Following this, two standard types of dynamic tests were performed.

First, planar plate tests (PPT) were conducted, where projectiles of hardened steel of 58 mm diameter and a thickness of 3 mm were fired against targets of 40 mm diameter and thickness of approximately 7 mm made of the materials to be investigated. The projectiles were accelerated with sabots in a gas gun to approximately 850 m/s in these tests.

The second series of tests were inverse Taylor tests (ITT). There, a projectile of hardened steel of 30 mm diameter and 30 mm thickness was fired onto a Taylor nail with a diameter of 6 mm and a length of 60 mm made of the material to be investigated. Here, two velocities of about 200 m/s and 400 m/s were used. The acceleration of the projectiles was again achieved with a gas gun.

The main objective of these experiments was to determine whether the materials show fragmentation and what size distribution is obtained.

The dynamic experiments were accompanied by camera recordings of the impact process. Two types of cameras were used. A PCO camera was used in nearly every experiment. The PCO camera can produce in total four images at predefined times or even eight images under the usage of double exposure. As

a second camera model, a SHIMADZU high-speed camera was available in some of the tests, which can take 200 images with a frame rate of 1 image each 2 μ s. During the experiments, we modified the exposure times for the cameras and also changed some details in the camera adjustment for improved sharpness of the images.

In the PPT experiments, the PCO camera had an orthogonal view onto the shot axis. In addition, a nearly frontal view onto the backside (that means against the shot axis) of the target was realized by using a mirror, which was observed with the cameras.

We executed the PPT and ITT experiments with a fragment collecting system. In the case of the PPT, the catcher consists of a series of chipboards and fiberboards which were arranged orthogonally to the shot axis. For the ITT, also ballistic soap has been used which gave the possibility to catch more fine particles and avoid the contamination of the fragments with fibers. The disadvantage of using soap is the subsequent usage of water which causes chemical changes to the surfaces of the fragments.

Every dynamic experiment has been conducted only one time (only for the CuFe sample 3114 the possibility for a pretest was given due to the manufacturing of a plate with differing thickness by the IFAM). That means repetitions are normally not executed, which would be useful for discussing the question of reproducibility. The reason for that is that the preparation of experiments is very time consuming, so that only one experiment could be conducted in one day. Sometimes it needed even more preparation time. Some of the experimental procedure is still in the process of further improvements.

For the definition of timescale, the trigger time of the cameras is used.

3.3 Results of Tensile Tests

Results of tensile tests of the samples which all have been sintered at 700 °C are shown and discussed in the following. Three samples were manufactured from one raw plate of material and were investigated under the same conditions. The applied strain rate was 0.001/s, as for the experiments conducted for the first lot.

It is obvious that all materials show a good reproducibility (figure 3.1 to figure 3.4). Often the curves follow each other in a congruent manner. Differences in the curves of one and the same material are given by variations in the maximum strain (the strain measurement is here based on the displacement measurement of the test machine). The highest value of 0.14 is found for the Cu samples, followed by the Fe (580 MPa) with a maximum strain between

0.08 and 0.095. Only half of this value is reached by the Fe (400 MPa) and less than a quarter by the CuFe.

The maximum tensile stress of more than 200 MPa is found for the Fe (580 MPa) samples, Fe (400 MPa) and Cu exhibit similar values of 135 MPa whereas CuFe reaches only less than 30 MPa.

The four materials investigated here show clear differences, which is evident if typical curves from figure 3.1 to figure 3.4 are unified in one single diagram (figure 3.5). The name of the curve specified in the legend is identical with that used in the previous figures.

In figure 3.6 the results of the corresponding materials of the first lot (see previous status report) are shown in a diagram of the same axis scaling. The new CuFe samples have a higher maximal tensile stress and elongation but they are in the tendency comparable. The Fe (400 MPa) is similar with a higher tensile stress. Larger differences occur in the case of the Fe samples which show almost a doubled strain and one third more maximal stress. The largest difference is found for the Cu samples which have a several times higher strain and maximal stress. The observed changes indeed serve the purpose of this project, as each material has a pronounced characteristic of its own.

The main parameters measured in the tests are summarized in the following tables 3.2a and 3.2b.

Table 3.2a: Mechanical properties of the old and new Fe samples derived from tensile tests. The elongations at break are given for the maximal tensile stress.

	New samples		Old samples	
Material	Fe 400 MPa	Fe 580 MPa	Fe 400 MPa	Fe 600 MPa
Elongation at break	0.03 0.03 0.04	0.10 0.08 0.08	0.05	0.05
Maximal tensile stress MPa	133 138 144	211 208 210	110	148

Table 3.2b: Mechanical properties of the old and new Fe samples derived from tensile tests. The elongations at break are given for the maximal tensile stress.

	New samples		Old samples	
Material	Cu 400 MPa	CuFe 580 MPa	Cu 400 MPa (800 °C)	CuFe 600 MPa
Elongation at break	0.14 0.14 0.14	0.01 0.01 0.01	0.02	0.02
Maximal tensile stress MPa	133 130 133	28 27 30	17	19

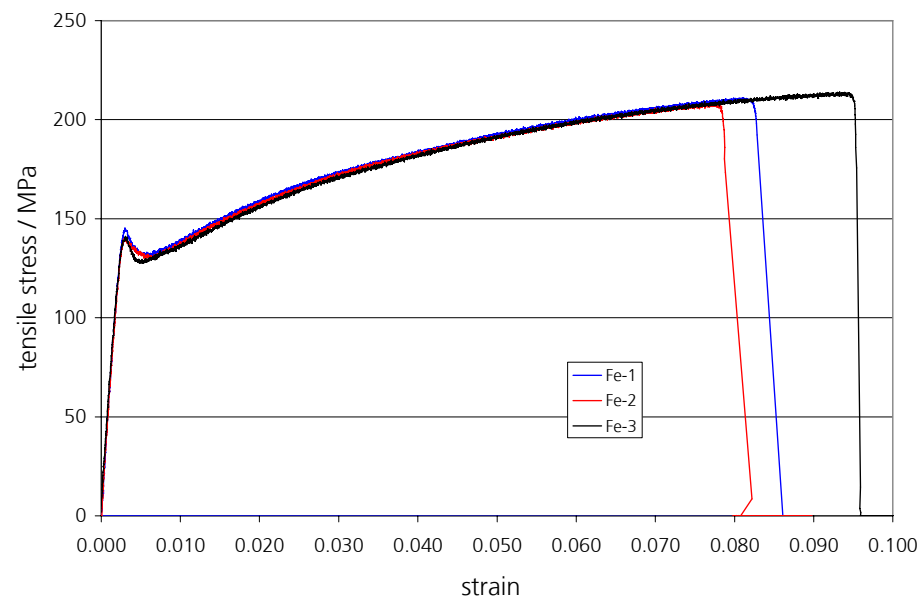


Figure 3.1: Stress-strain curves of three Fe samples (700 °C/580 MPa).

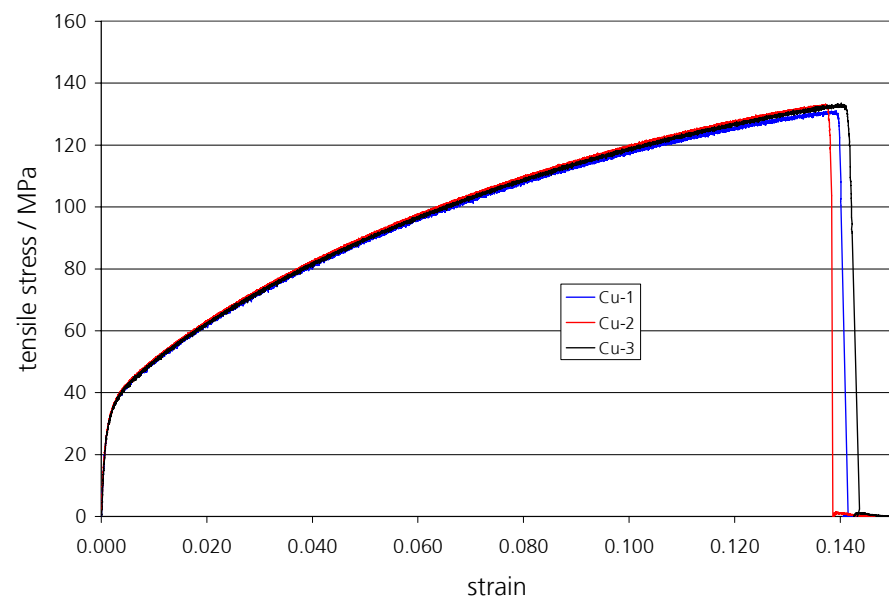


Figure 3.2: Stress-strain curves of three Cu samples (700 °C/400 MPa).

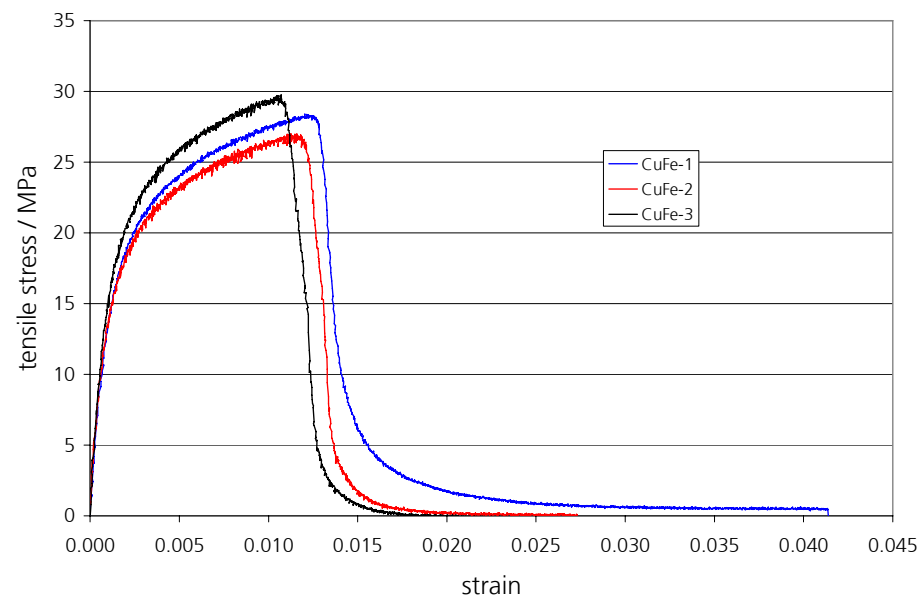


Figure 3.3: Stress-strain curves of three CuFe samples (700 °C/400 MPa).

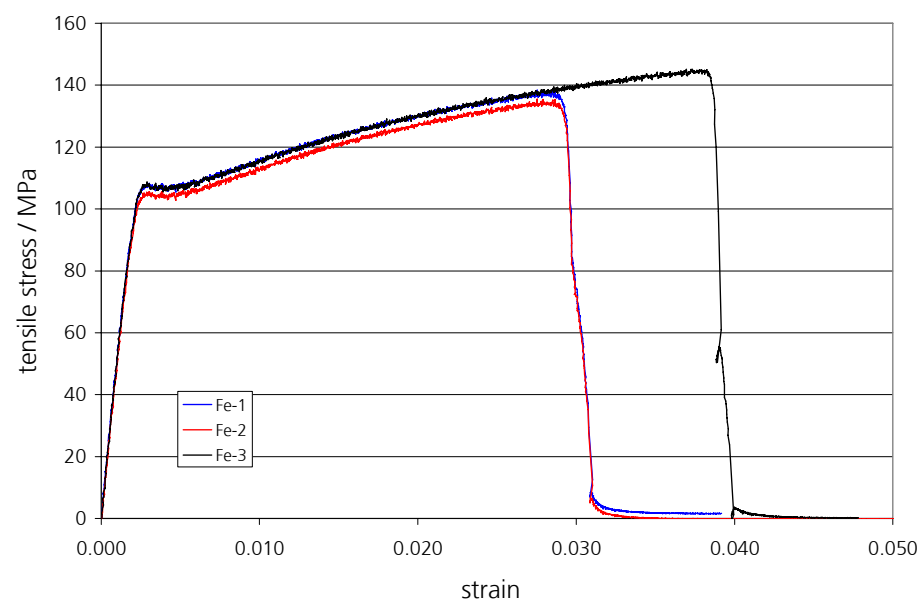


Figure 3.4: Stress-strain curves of three Fe samples (700 °C/400 MPa).

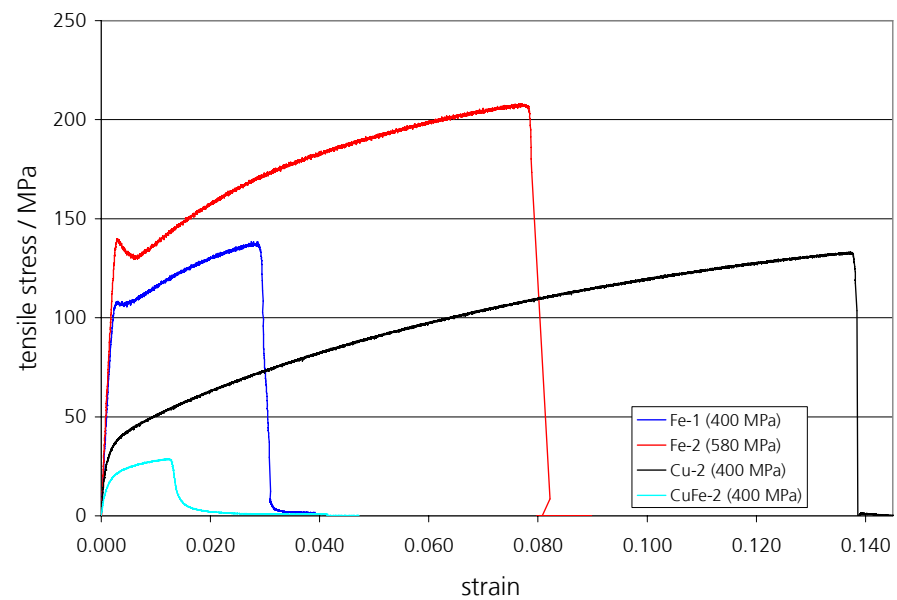


Figure 3.5: Stress-strain curves of the new four different materials.

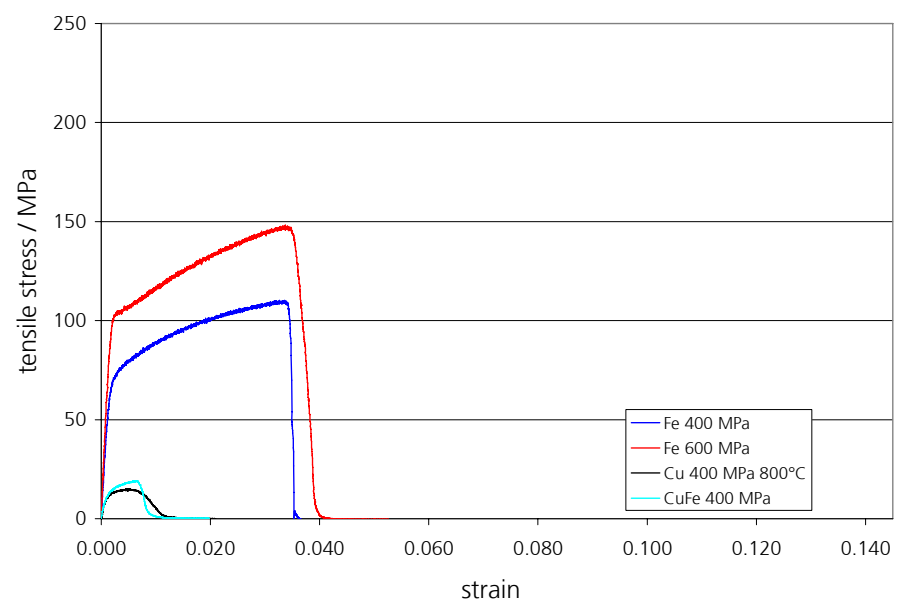


Figure 3.6: Stress-strain curves of the four materials manufactured with the old technique (these results have been already described in the 2nd Quarterly Progress Report I/2008).

3.4 Results of Planar Plate Tests

Selected camera recordings of the tests are available on the CD attached to this report. For a convenient reference, the identification numbers of the tests are listed in the following text. Details of the experimental conditions are given in table 3.3.

In the following, a sequence of single images of a test with a CuFe sample (3117) at an impact velocity of 853 m/s is shown to demonstrate the general features of the impact process.

In figure 3.7, the setup of the test is shown, in which the target is at rest on a glass holder, which also carries the trigger pin. With the trigger pin the camera recordings are started. Figure 3.8 shows the first beginning of the formation of fine fragments, which develop out of the perimeter of the target. The further development of the fragment cloud is shown in the figures 3.9 and 3.10, which are taken 8 μ s and 14 μ s later. In the center of the backside no fine fragments are visible. In figure 3.10, however, fine lines of spallation fissures are observable on the backside of the target. Figure 3.11 shows the later time, in which parts of the projectile become visible.

A summary of essential characteristics which were identified from the series of photographs of the experiments are listed in table 3.3 and are discussed in the following.

In general, fragmentation can be observed in every experiment. But one can distinguish between two different size ranges of fragments:

- A large fraction with a range of several mm up to centimeters (only a few parts can be formed out of one sample), and
- a fine fraction, which is below several mm and goes down to the μ m scale.

The fine fraction can be observed immediately after the impact. The side of the target hidden by the projectile produces small fragments, which build a surrounding ring around the target. This fragment cloud is then expanding under an angle of approximately 45 degrees relative to the shot axis. The expansion of the fragment cloud exposes different sizes of single particles which can extend over several pixels in one image. From these pixel sizes a real size of 1 mm to 3 mm, depending on the experiment, can be derived. Even smaller particles are present, which are indicated by fast changes of the contrast in the images.

The large fraction of fragments is observed indirectly by inspecting the spallation behavior of the backside of the target. Several μs after the impact fissures begin to increase over the backside, their thickness and clearness also becomes more expressed with increasing time. They indicate spallation of the sample and should normally only be characteristic in the flat surface region of the backside.

In every experiment both fragmentation size intervals are present. But depending on the material, differences are detectable. The impact time is nearly identical in all experiments. The times where spallation processes are observable shows larger differences, which are caused by differences of the material properties. The time, in which fragment generation of the backside takes place ranges from 12 μs (3115, CuFe, 400 MPa) to 120 μs (3116, Fe, 580 MPa).

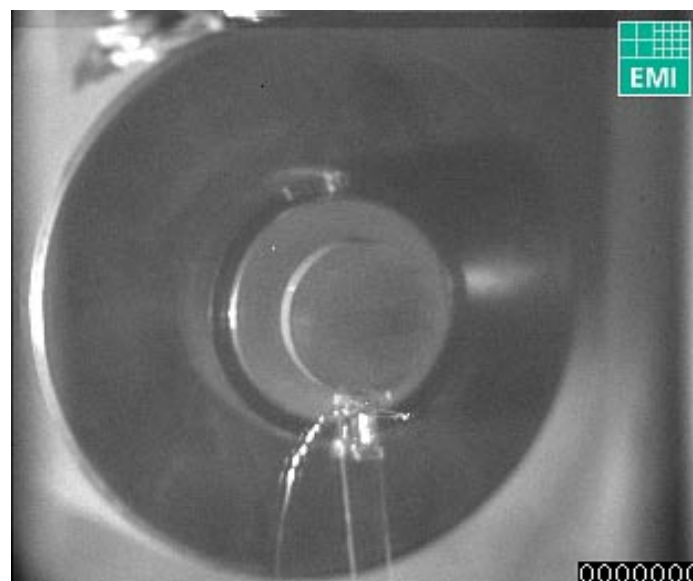


Figure 3.7: View onto the backside of the target, the projectile just leaving the muzzle of the gun. Trigger time 0 μs (indicated by the numbers in the right bottom corner).

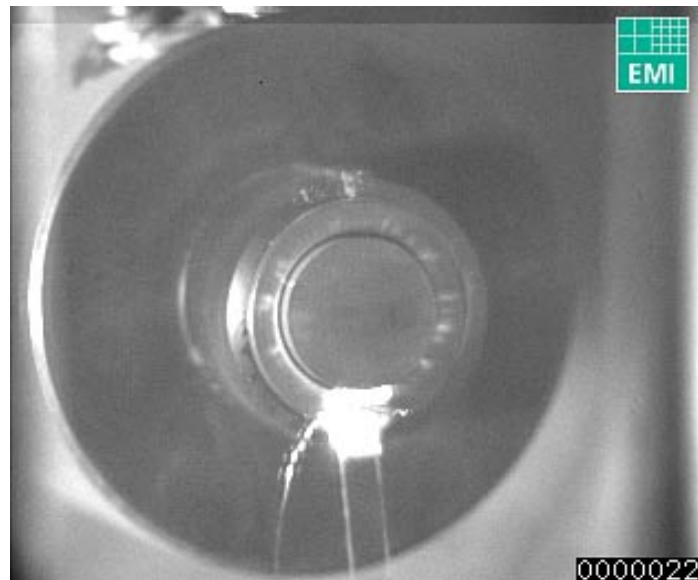


Figure 3.8: View onto the backside of the target. The impact has just started. One can observe a thin contour around the target, from which several "rays" of finest fragments escape. Trigger time 22 μ s.

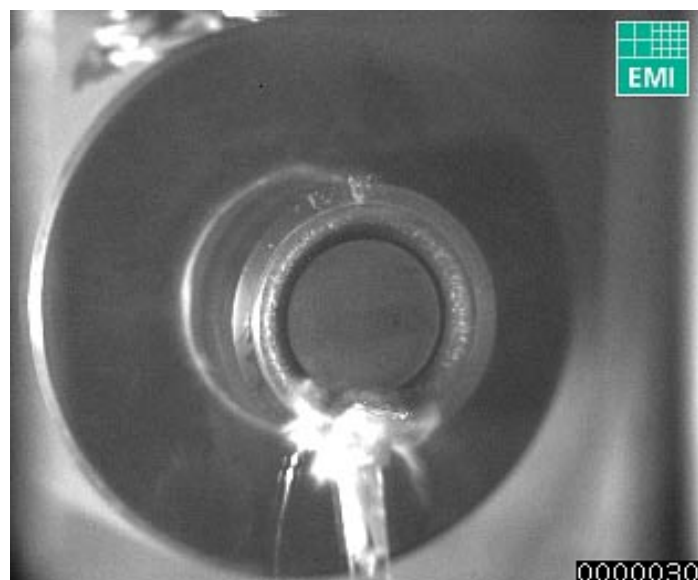


Figure 3.9: The surrounding contour develops into a ring of fragments. Trigger time 30 μ s.

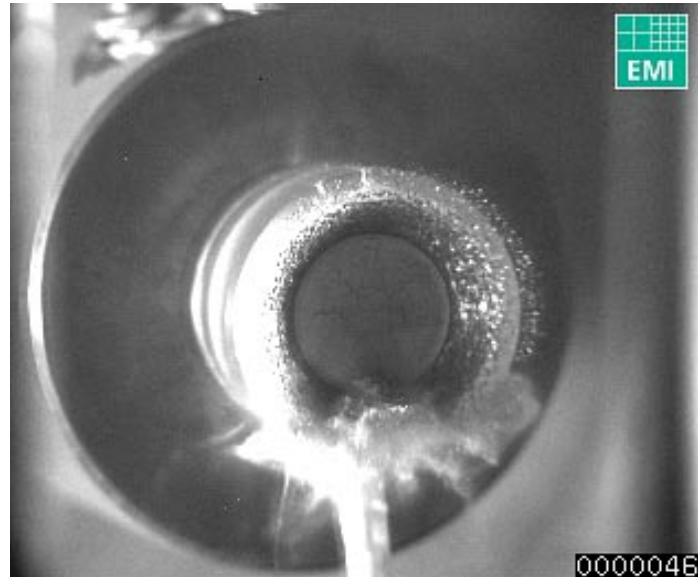


Figure 3.10: The cloud of fine fragments is expanding. At the backside of the target spallation fissures are visible. Trigger time 46 μ s.

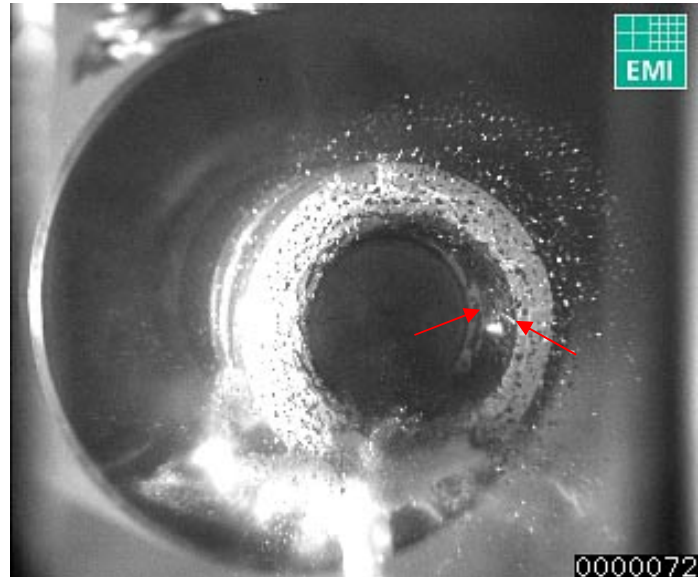


Figure 3.11: The fragment movement is going on. Here an outer concentric (arrows), dark structure is becoming visible. It is the ring of the projectile plate which is sheared off during the impact by the inertia of the heavy target plate (the mass of the projectile plate is smaller, the diameter larger than that of the target plate). Trigger time 72 μ s.

Table 3.3: Overview over the camera recordings in the PPT experiments. The time t is the time after the trigger has been started.

Measure- ment	Material	Impact velocity m/s	Impact at time t μs	Start of spallation of backside at time t μs	Shimadzu *.jpg-images (alternatively PCO-camera results)
3114 (Pretest)	CuFe 400 MPa (Pretest)	836	22	30	Central section with 15 mm diameter shows spallation and fragments into 4 parts until $t = 50 \mu\text{s}$. At $42 \mu\text{s}$ nearly the complete backside spallates. The observable fine fragments from the outer circle have a size of 1 mm and below.
3115	CuFe 400 MPa	888	22	36	Central section with 29 mm diameter shows spallation and fragments into several parts until $t = 72 \mu\text{s}$. At $44 \mu\text{s}$ the outer ring shows fragmentation. The observable fine fragments from the outer circle have a size of 2 mm and below.
3116	Fe 580 MPa	836	22	26	Central section with 30 mm diameter shows spallation and fragments into several parts until $t=146 \mu\text{s}$. The observable fine fragments from the outer circle have a size of 3 mm and below.
3117	CuFe 400 MPa	853	20	32	Central section with 35 mm diameter shows spallation and fragments into several parts until $t=80 \mu\text{s}$. The observable fine fragments from the outer circle have a size of 1 mm and below.
3118	Fe 400 MPa	850	-	-	PCO: Spallation of the central backside
3120	CuFe 400 MPa	323	-	-	PCO: Spallation of the central backside (image 4)

In figure 3.12 to figure 3.15, the fragmentation behavior of the most unstable material (CuFe, 400 MPa) is shown in comparison with the most stable material (Fe 580 MPa) at two different times after the impact.

At both times a nearly identical progress of the fragmentation is seen, but it can clearly be recognized that the fragmentation cloud of the Fe sample has a lower density.

The fragmentation of the center area of the backside of the Fe sample differs from the CuFe sample by a nearly complete spallation of the backside. The backside behaves more as a unit instead of sub-fragmentation in large particles up to this moment.

The existence of different fragment densities in the cloud of fine fragments can also be observed in the series of the PCO images, which were taken orthogonally to the shot axis (figures 3.16 to 3.21). The same experiments are shown as discussed with the SHIMADZU images, the time values assigned to the PCO images however differ due to individual time bases of the camera trigger settings. It is evident, that the density of particles in the Fe fragment cloud is smaller compared to the CuFe sample, while the particles in the CuFe fragment cloud are smaller than in the Fe fragment cloud. In the front section of the CuFe fragment cloud (figure 3.17), a "dusty region" indicates particles with a size near the resolution of the camera. These particles could not be observed in the SHIMADZU images due to a lower spatial resolution under the specific imaging conditions. Cu samples exhibit a reduced amount of fragments (figures 3.20 and 3.21).

The expansion angle of nearly 45 degrees which is similar for both samples indicates a velocity component of the fragments orthogonal to the shot axis which is comparable with the velocity component in the shot axis.

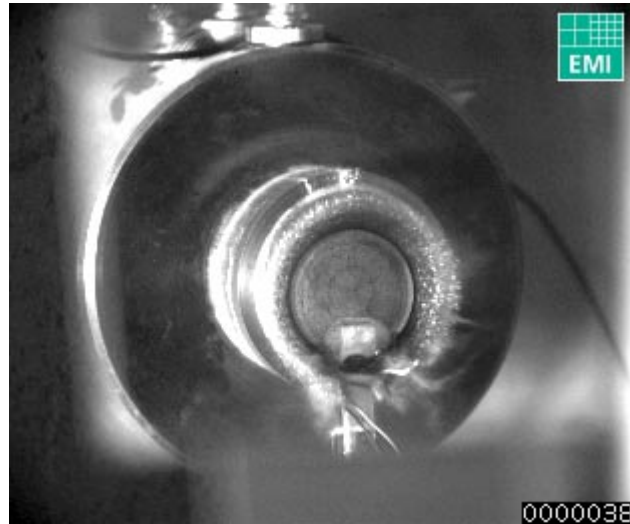


Figure 3.12: CuFe sample (3114). A cloud of fine fragments is observable. At the backside of the target spallation fissures are visible. Trigger time 38 μ s.

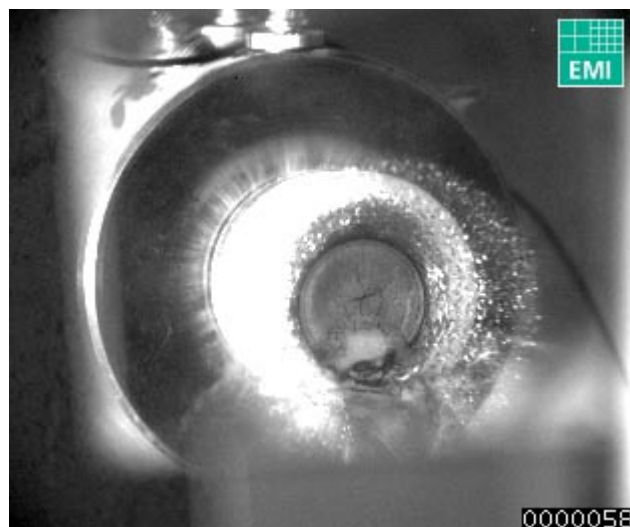


Figure 3.13: CuFe sample (3114). The cloud of fine fragments is expanding. At the backside of the target spallation fissures are visible. Trigger time 58 μ s.

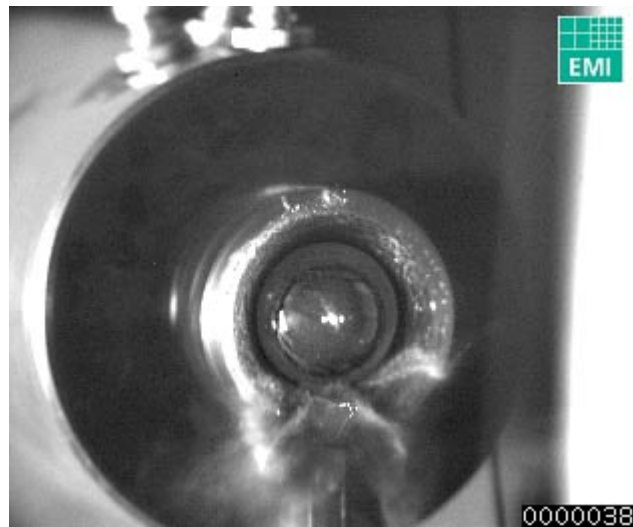


Figure 3.14: Fe sample (3116). A cloud of fine fragments is observable. At the backside of the target spallation is visible. Trigger time 38 μ s.

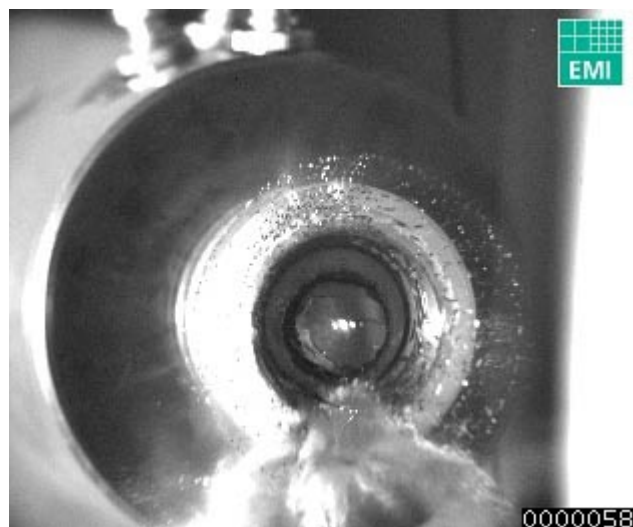


Figure 3.15: Fe sample (3116). The cloud of fine fragments is expanding. At the backside of the target spallation process moves on. Trigger time 58 μ s.

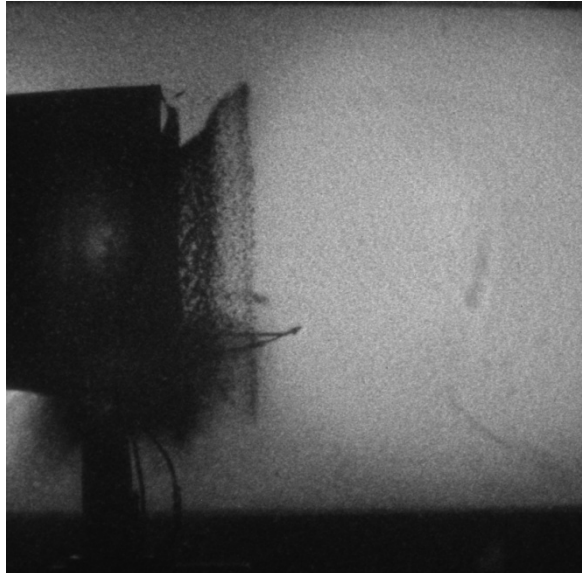


Figure 3.16: CuFe sample (3114, image 2). The cloud of fine fragments is visible. Trigger time 30 μ s.

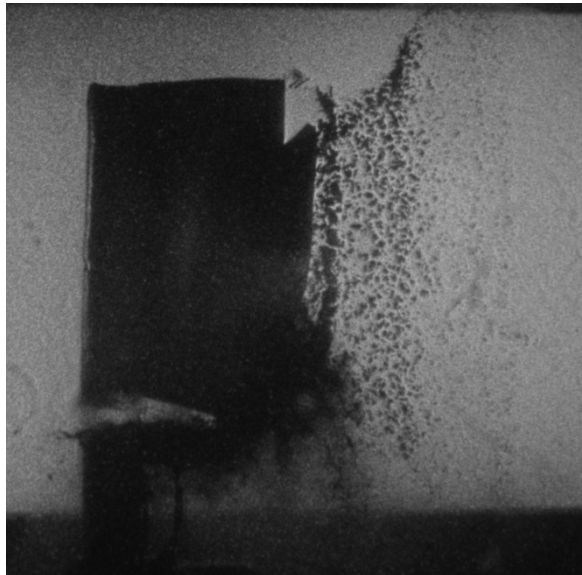


Figure 3.17: CuFe sample (3114, image 3). The cloud of fine fragments is expanding. There are very fine fragments in the foremost part of the fragment cloud. Trigger time 70 μ s.

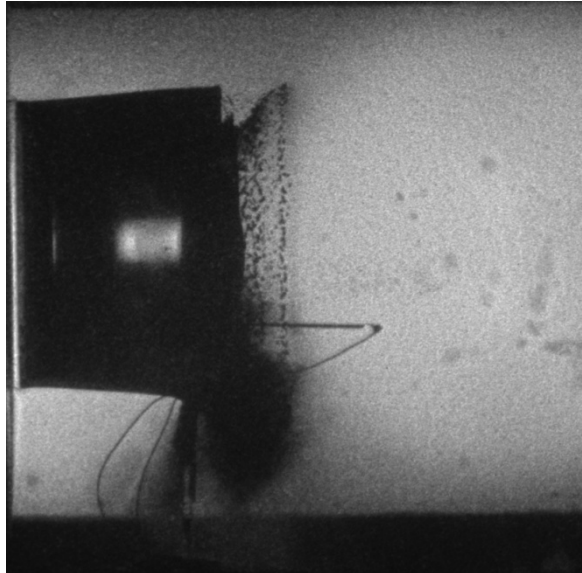


Figure 3.18: Fe sample (3116, image 2). The cloud of fine fragments is visible. Trigger time 25 μ s.

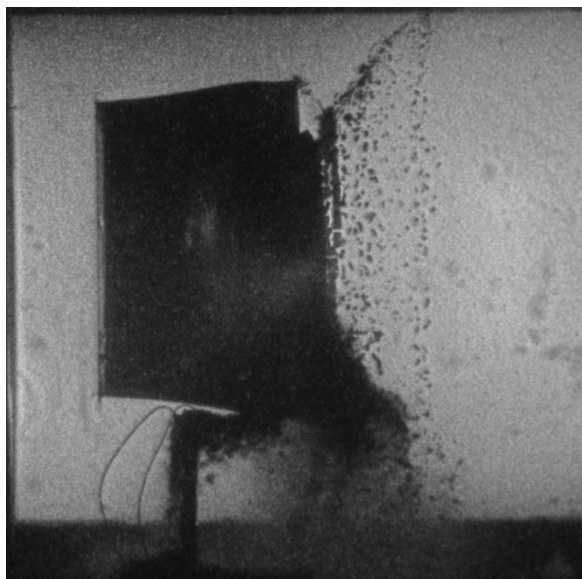


Figure 3.19: Fe sample (3116, image 3). The cloud of fine fragments is expanding. Regions with different density occur. Trigger time 50 μ s.

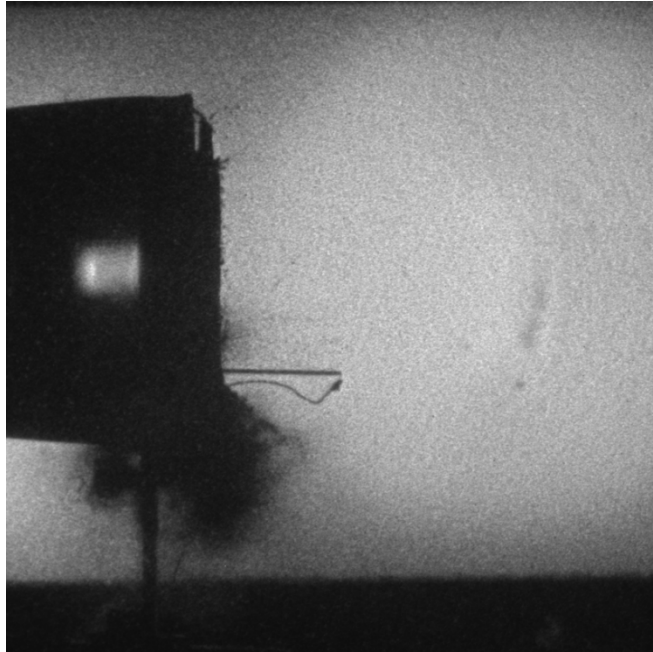


Figure 3.20: Cu sample (3115, image 2). Trigger time 25 μ s.

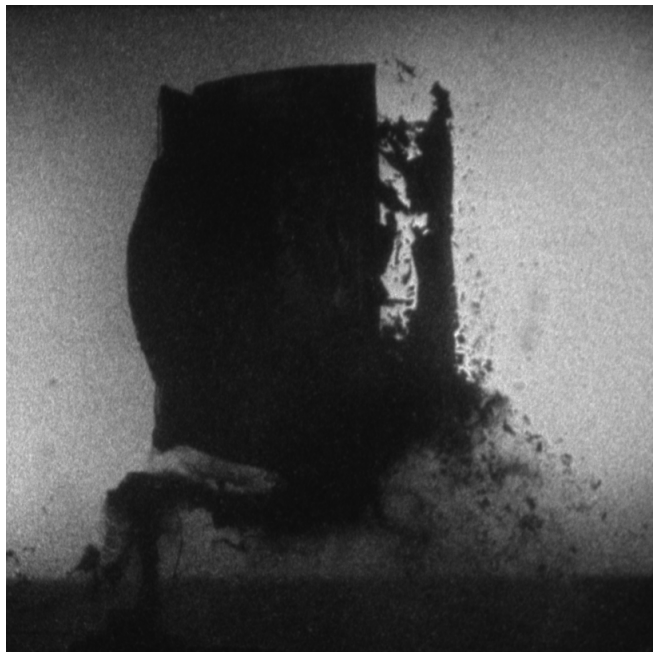
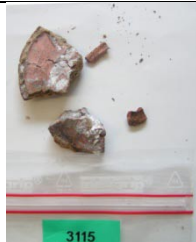


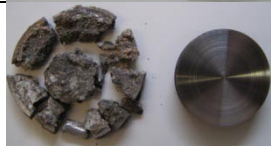



Figure 3.21: Cu sample (3115, image 4). The number of fragments is reduced compared with Fe and CuFe samples. Trigger time 75 μ s.

Further information on the fragmentation behavior can be derived by an inspection of the collected fragments of each experiment.

The fragment collecting system for the PPT was based on the usage of the fiberboards already mentioned in the overview. In table 3.4, details of the experimental conditions and also photographs of the collected fragments are shown.

Table 3.4: Overview over collected fragments in PPT experiments. The label indicating the number of the measurement has a size of 12 mm x 31 mm, the target a diameter of 40 mm (shown for measurement 3118, right side).

Measure- ment	Materi al	Impact velocity m/s	Collecting rate	
3115	Cu 400 MPa	888	0.36	
3116	Fe 580 MPa	836	0.88	
3117	CuFe 400 MPa	853	0.57	
3118	Fe 400 MPa	850	0.76	
3120	CuFe 400 MPa	323	0.83	

In the table in the fourth column, the “collecting rate” is listed. The collecting rate is defined as the ratio of the total mass of the collected fragments in relationship to the mass of the target before the experiment was conducted.

The collecting rate gives an impression of the efficiency of the fragment collecting system, the value of 1 would be reached, if 100 % of the original sample material is collected. The collection rate expresses under our conditions the amount of fragments, which could be found without deeper search for the particles in the series of fiberboards. All fine fragments are hard to detect. Also the part of fragments which is not reaching the fragment collecting system is lost, if it could not be found in form of large fragments in the measurement chamber. In this sense, the missing rate (to fulfill 100 %) characterizes the fine fraction. This is not really exact because particle distribution statistics would only be possible if we have collected nearly 100 % of the original mass but it is possible to derive tendencies if one assumes, that the missing mass is not given by of few large fragments but by a large amount of fine particles.

The distance between the fragment collecting system and the target is 40 cm. If under this geometric conditions an expanding fragment cloud has a higher diameter as the entrance hole of the fragment collecting system, this part of the fine fragments is lost. In this sense, the missing part of the collected fragments is the fine fraction.

A further assumption, which is made in all results based on the data of the fragment collecting system, is, that the second impact onto the collector system has a negligible influence to the fragment distribution because the impact energy of the second impact is much smaller than the primary impact of the projectile.

The characteristics of the images given in table 3.4 can be summarized as follows.

- In all experiments (except 3116) large (> 3 mm) and fine fragments (< 1 mm) could be collected.
- The Cu (3115) or CuFe (3117) samples at high impact velocities have a significantly reduced collection rate, or, following the arguments listed above, a higher degree of fine fragments.
- A larger amount of smaller fragments is observable with the CuFe samples (3117, 3120).
- The most stable material (Fe, 580 MPa, 3116) shows large fragments with a sharp outer shape, so that it very easily could be composed

again. This possibility is obviously reduced with the Fe (400 MPa, 3118) or Cu (3115).

- The number of smaller fragments is increasing with the less stable CuFe samples (3117). If here the impact velocity is reduced (3120), then the size of larger fragments increases and the collection rate is increasing.

These observations lead to the following tendencies: The more stable the material, the less is the amount of smaller fragments. The higher the impact velocity, the smaller is the generated mean fragment size.

What one could observe directly in the series of photographs, is also visible in the collected fragments. Both experimental observations are corresponding with the general assumptions one would have for these processes.

3.5 Results of Inverse Taylor Tests

The ITT experiments were accompanied by camera recordings only in the orthogonal direction of view relative to the shot axis. In some of these experiments, the first usage of soap as a fragment collecting medium was tried.

In addition, double exposure of the images was used. Here, only the PCO camera recordings are discussed. The first two and the last two images are shown.

With an impact velocity in the region of 200 m/s, the Taylor nails show mainly deformation (figures 3.23 and 3.24). In the following figures, the first and the last two of the PCO images are shown, they are arranged in column form with the first two in the top and bottom position left and the last two in the top and bottom position right).

Only the CuFe sample exhibits a production of finest fragments (figure 3.23; in the two last images a "dusty region" around the deformation area is visible). In the collector system, the sample was found broken in several parts (figure 3.22).

The consequence of these experiments is that the impact velocity was chosen to small for a generation of fragments. Therefore, the impact velocity has been doubled (figures 3.25 to 3.27). Under this condition, all samples showed deformation as in the cases before but the shortening of the sample was accompanied by an expressed generation of fragments.

The fragments escape nearly orthogonally to the shot axis (figures 3.25 to 3.27, images 3 and 4). Only a small amount of these fragments could be captured in our fragment collection system. The size of these fragments is partially beyond 1 mm or even much smaller.



Figure 3.22: CuFe Taylor nail sample. Top: an original sample with a size of 6 mm diameter and a length of 60 mm. Bottom: fragments of the Taylor nail (3121) after an impact with a velocity of 217 m/s.

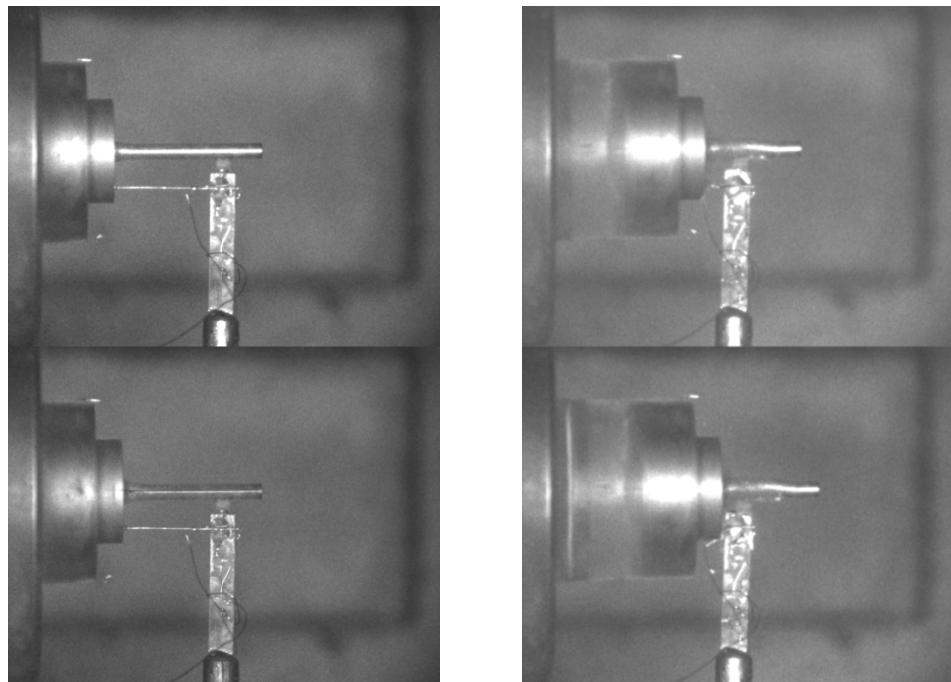


Figure 3.23: CuFe Taylor nail sample (3121, images 1, 2, 7, 8). The deformation of the Taylor nail can be seen. Trigger times 15 μ s, 30 μ s, 150 μ s, 180 μ s. Impact velocity 217 m/s.

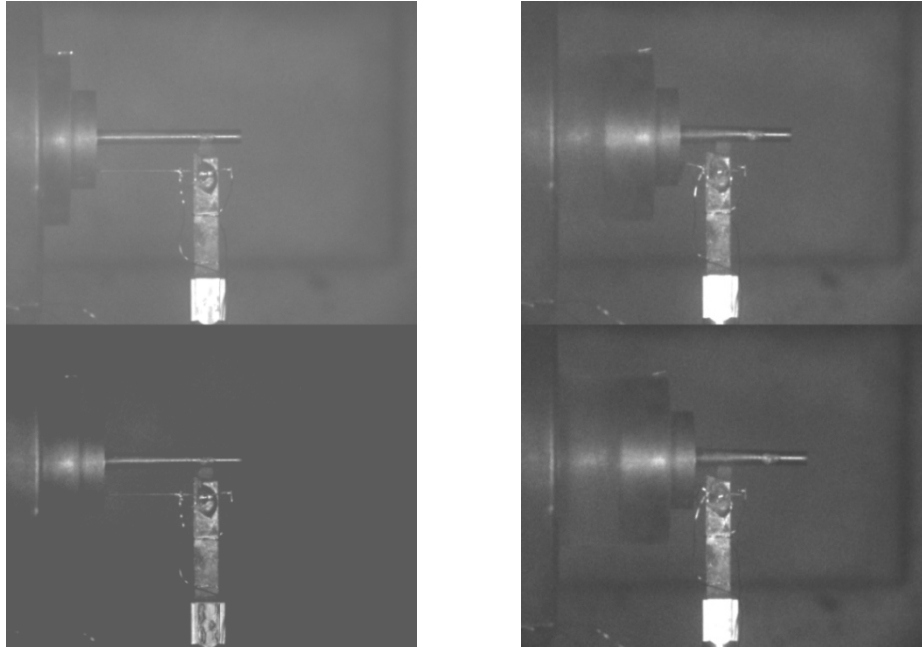


Figure 3.24: Fe Taylor nail sample (3123, images 1, 2, 7, 8). The deformation of the Taylor nail can be seen. Trigger times 15 μ s, 30 μ s, 150 μ s, 180 μ s. Impact velocity 207 m/s.

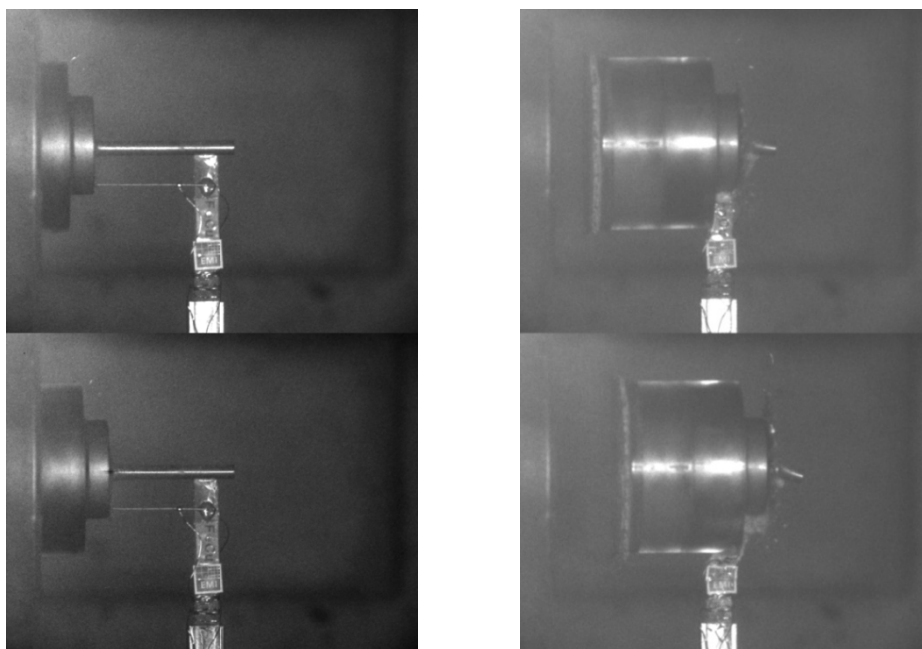


Figure 3.25: CuFe Taylor nail sample (3128, images 1, 2, 7, 8). The deformation of the Taylor nail and the generation of fragments can be seen. Trigger times 15 μ s, 30 μ s, 150 μ s, 180 μ s. Impact velocity 387 m/s.

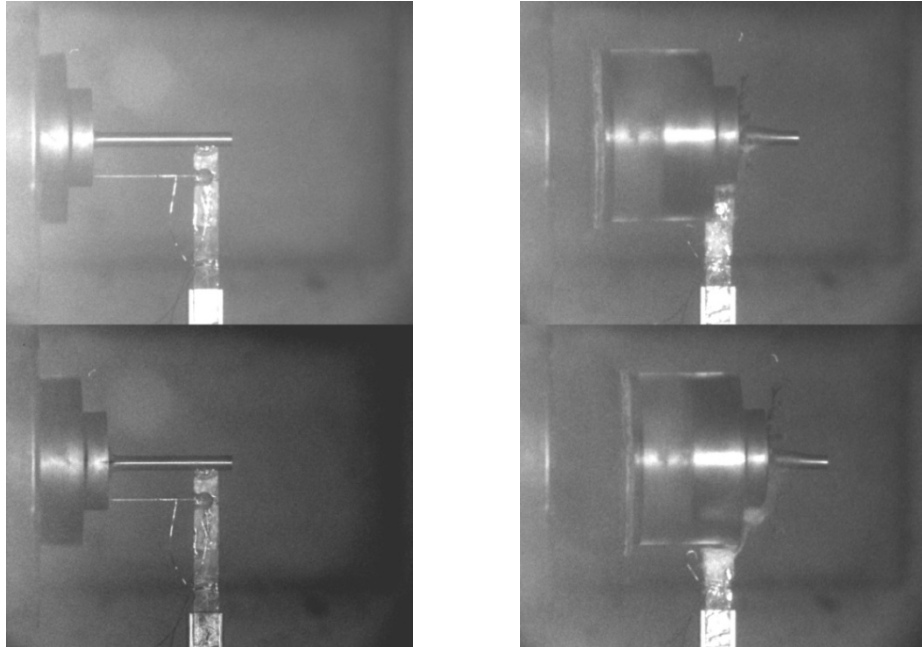


Figure 3.26: Fe Taylor nail sample (3129, images 1, 2, 7, 8). The deformation of the Taylor nail under the generation of fragments can be seen. Trigger times 15 μ s, 30 μ s, 150 μ s, 180 μ s. Impact velocity 398 m/s.

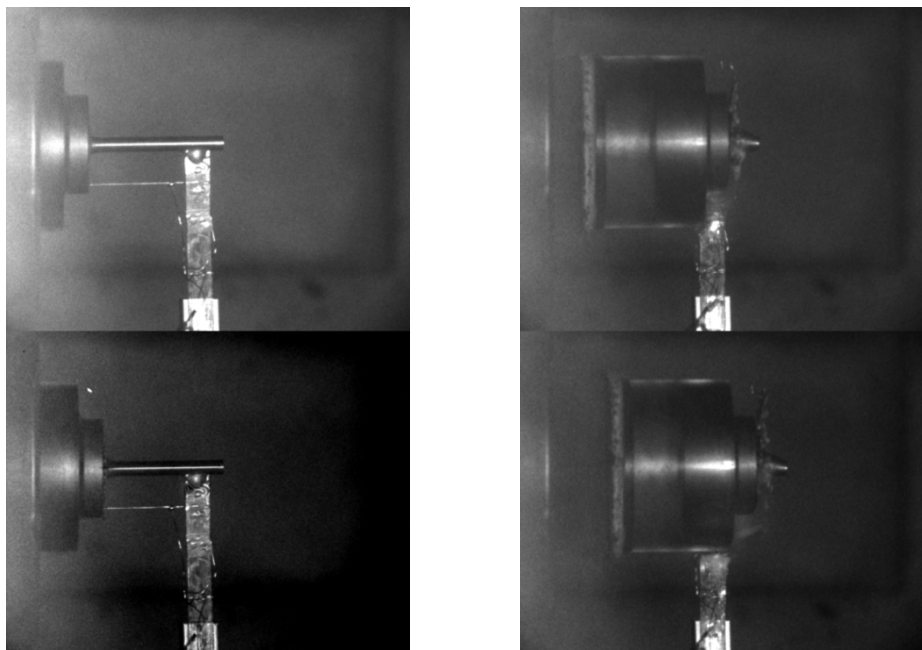


Figure 3.27: Cu Taylor nail sample (3130, images 1, 2, 7, 8). The deformation of the Taylor nail under the generation of fragments can be seen. Trigger times 15 μ s, 30 μ s, 150 μ s, 180 μ s. Impact velocity 432 m/s.

3.6 Conclusions and Consequences for Future Tests

Usage of cameras

Both camera perspectives have advantages and disadvantages. The expansion angle in PPT experiments can only be observed in the orthogonal direction, but this shadows and overlays fragments in the fragmentation cloud. Spallation processes on the center of the backside of the target could not be observed. If from this region fragments would expand, they would also overlap with the fine fragments in the fragmentation cloud.

The expansion angle might be a characteristic function of the impact velocity and the sample material properties (the phenomenon should not be caused by the cut off shear process of the overlooking region of the projectile (the experimental setup needs projectiles with a larger diameter than that of the targets because the projectile triggers the velocity measurement)).

The perspective against the shot axis is useful for observations of the center region in the PPT experiments. The spatial expansion of the fragmentation cloud of fine fragments is characterized only in a qualitative way. In the case of ITT experiments, this perspective would have the advantage of a good observation of the fine fragments at sufficiently high impact velocities. This arrangement has been not used so far, but it will be used in future tests.

The camera technique gives an excellent overview of the spatial extension of fragment clouds, contractions of the sample and spallation behavior in situ (and as a function of time), but not a complete information about the fragmentation behavior due to the limited particle size resolution of the cameras. As estimation from the ITT images taken with the PCO camera one can derive that an object of a length of 60 mm is represented by 220 up to 260 pixels. One single pixel would therefore be identical to an object size of approximately 0.25 mm. A size measurement of an object is possible when different contrasts over the object can be distinguished which might be the case if an object is represented by at least two pixels in one dimension (0.5 mm) or even better by three pixels (0.75 mm). This estimation shows that the shape of a fragment cannot be detected, if not at least six pixels are accompanied (2×3), so that fragment sizes could not be derived from the images for real particles smaller than 0.75 mm (in one dimension; even in this cases the possible error of this "measurement" is one pixel, that means 30 % to 50 %(!)). The field of view of the cameras has not a squared format, so that the directions are not equivalent, what reduces the real object resolution again. If one observes the target at larger effective distances (over a mirror, in the view against the shot axis), the resolution is decreasing by a factor of 1.5 to 3 compared to the PCO camera resolution discussed above. A smallest resolution in the 1 mm region is not sufficient to derive particle size distributions of the fine fragments from the

images. A further improvement is not possible due to technical limitations (chamber size, spatial resolution of the camera).

Collection of fragments

Therefore, the collection technique should be improved so that the collection rate reaches 100 %. This could be done by a modified arrangement of the fragment collecting system in combination with the usage of ballistic soap as collector medium. The fragments could then be analyzed by sieve analysis. The number of fine fragments is high enough for a valid statistics derived from the fragment distribution. This would give the chance to characterize fragmentation behavior as function of the impact velocity.

VISAR

The usage of the VISAR would give quantitative insights in the dynamic behavior of the samples. We plan to use VISAR in addition to camera recordings and fragment collection in future tests.

Materials

If the materials are impacted with sufficient energy, they produce a lot of fragments. These fragments could reach diameters in the order of 0.1 mm, which is comparable with the primary particle diameter.

For these fine fragments – beside the characterization with the particle distribution discussed above – a microscopic analysis will be done. Here, the question of the fragmentation mechanism will be important. For the simulations a fragmentation on the sintered contact areas is important.

4 Structure Generator

4.1 Features and Statistics of the Investigated Micrographs

4.1.1 Pure Iron and Pure Copper Material Samples

In figure 4.1, four different cut images of pure copper samples from the first lot of delivered material are shown. These images only show a rudimentary granular structure which is not amenable to our approximation of microstructures as polyhedral cell complexes. The same is true of the pure iron material samples shown in figure 4.2. They show a cellular or foam-like structure which cannot be used as a basis for an approximation using convex polyhedra. Methods other than POLYGRAIN have to be applied to these materials.

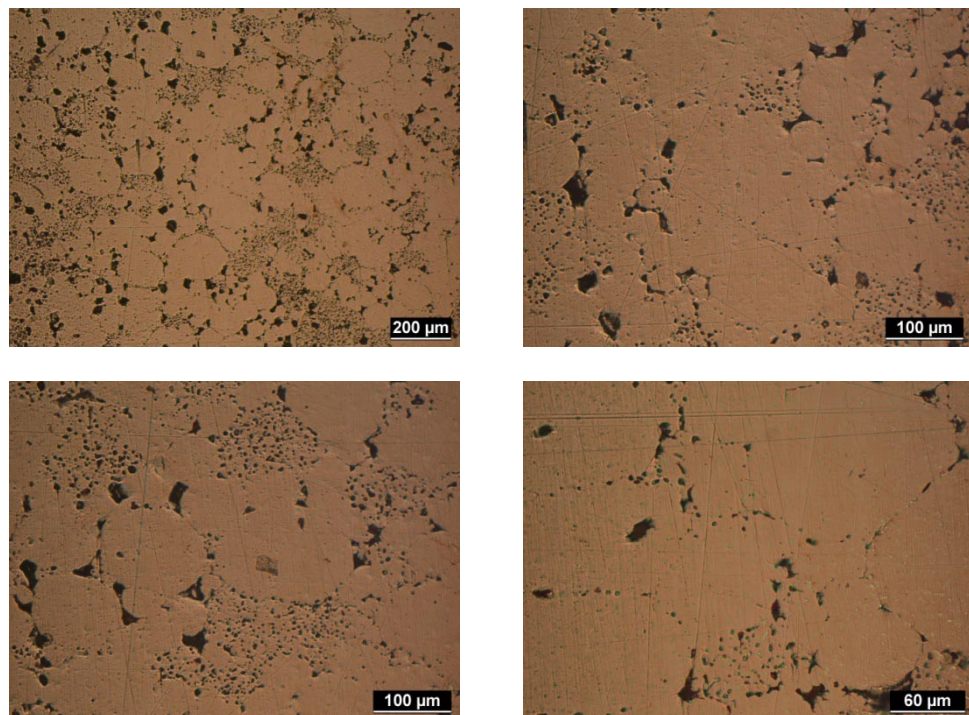


Figure 4.1: Four different typical micrographs of copper material samples from the first (preliminary) lot.

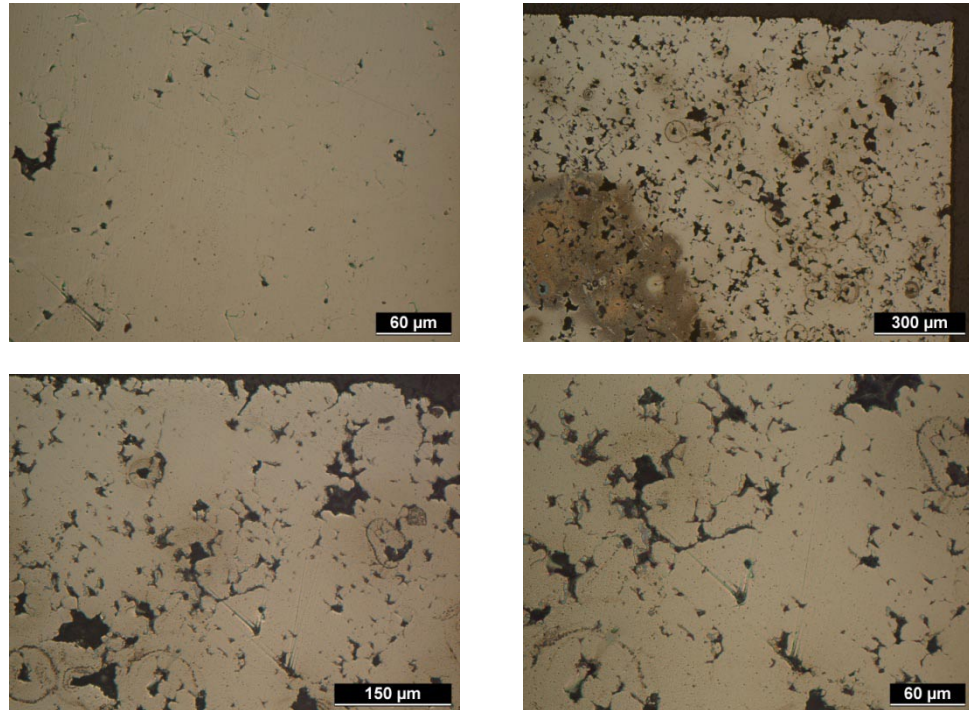


Figure 4.2: Four different typical micrographs of pure iron material samples from the first (preliminary) lot.

4.1.2 Mixed Iron/Copper Material Samples

In figure 4.3, we show the micrographs that were chosen for a statistical analysis and the corresponding idealizations of the grain boundary patterns that were done by hand. Figure 4.4 shows the corresponding statistics of grain area and grain shape. The shape parameter considered here is defined as

$$S = 2\sqrt{\pi}\sqrt{A}/U$$

where A is area of the cut grain geometry and U the perimeter. Note, that $S = 1$ for circles and $S < 1$ for any other geometry. For example, a rectangle with edge length ratio of 4 has a value of $S = 0.71$, while a square has $S = 0.88$. The evaluation of grain pattern has been done with the KS 300 software from ZEISS. As the different materials or pores could not be distinguished in this approach the statistics comprises all patterns in the micrographs. The moments of the distributions of area and perimeter were used as input for the iterative adaption of the POLYGRAIN geometry model in chapter 4.5.

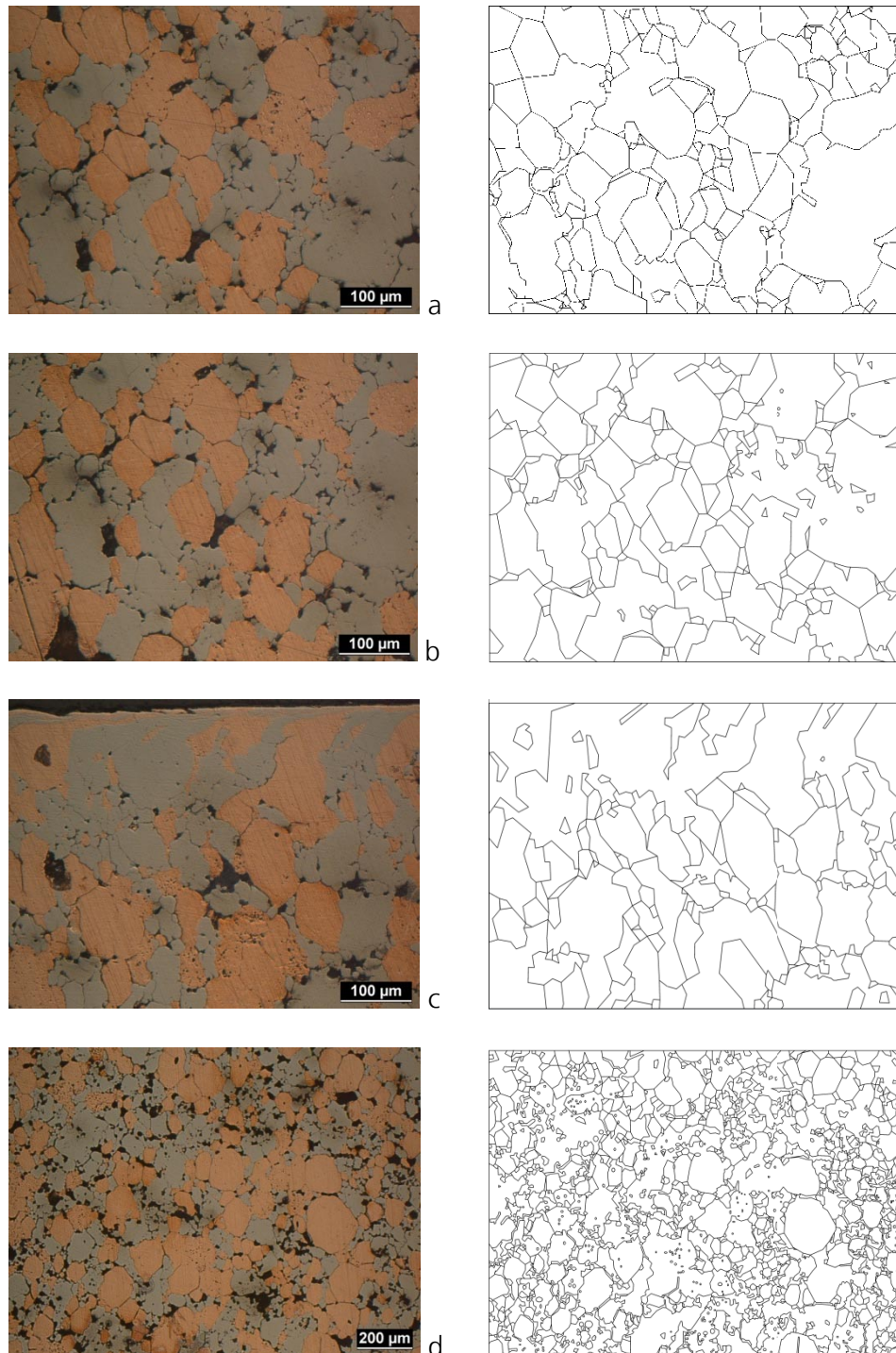


Figure 4.3: These micrographs of FeCu samples from the first (preliminary) lot were statistically analyzed after being traced out by hand. Total number of grains: 214, 213, 146, 1264 (top to bottom).

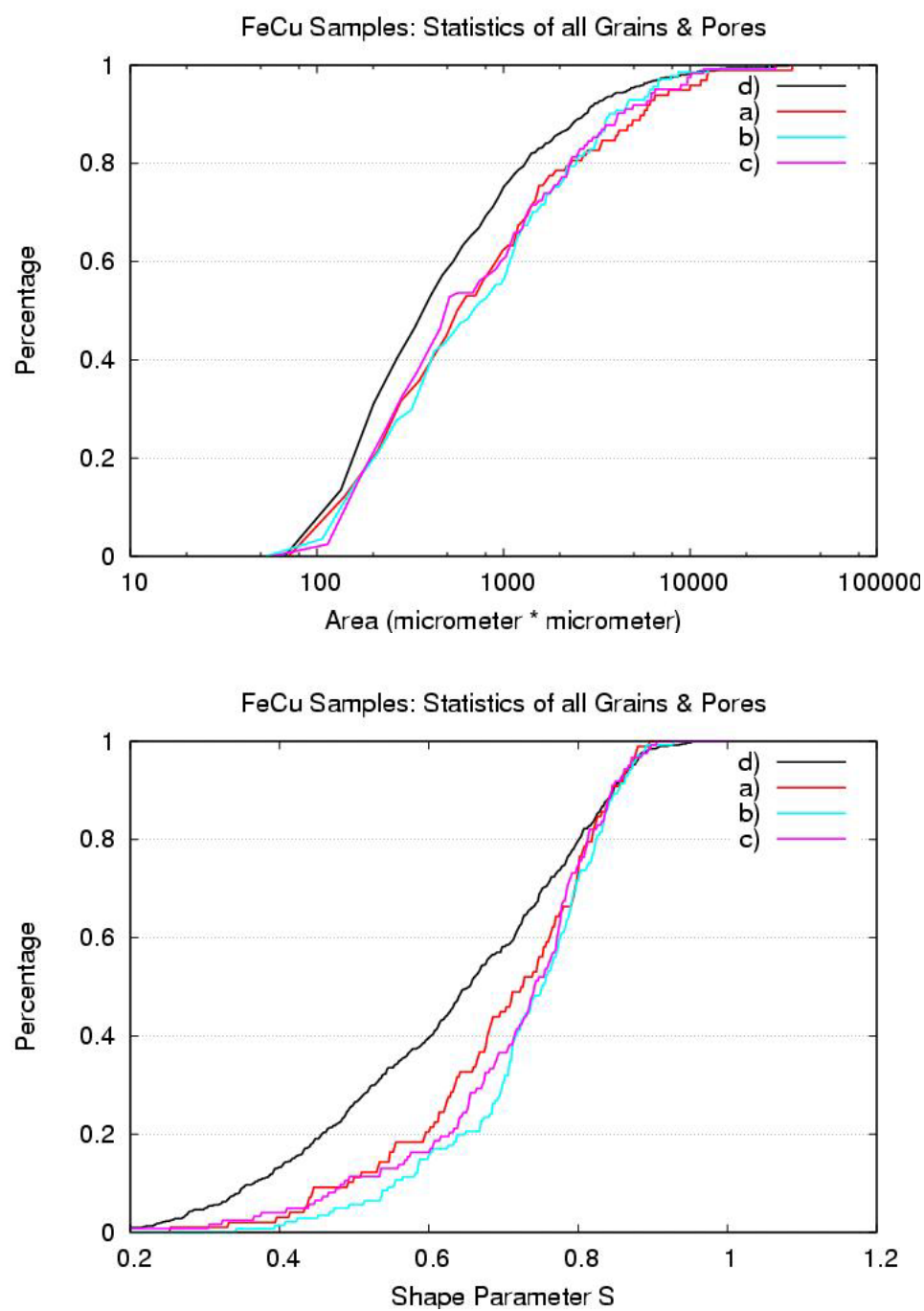


Figure 4.4: Cumulative distribution of grain area and shape value. Grains with area smaller $100 \mu\text{m}^2$ were discarded from statistics. 50 % of counted grains have a size between about $500 \mu\text{m}^2$ and $20,000 \mu\text{m}^2$ and shape parameters $S > 0.7$.

4.1.3 Additional Statistical Data

The semi-automated image processing as described above did not provide individual statistics for the geometries associated with the different constituents and the pores of the material.

Further exemplary evaluation of the same micrographs was therefore attempted through measuring out the geometries by hand. Figure 4.5 shows as an example the manual determination of the two major and minor semi-axes of grains, which are to a reasonable approximation perpendicular to each other. The semi-axes were measured only for the larger patterns while the smaller patterns were just counted and sorted into two size ranges.

Assuming ellipses as basic approximations for the true irregular geometries, the area and perimeter distributions were estimated selectively for both material constituents. The result is shown in figure 4.6. The discrepancy between these results and those from figure 4.4 is due to the individual measurements by hand.

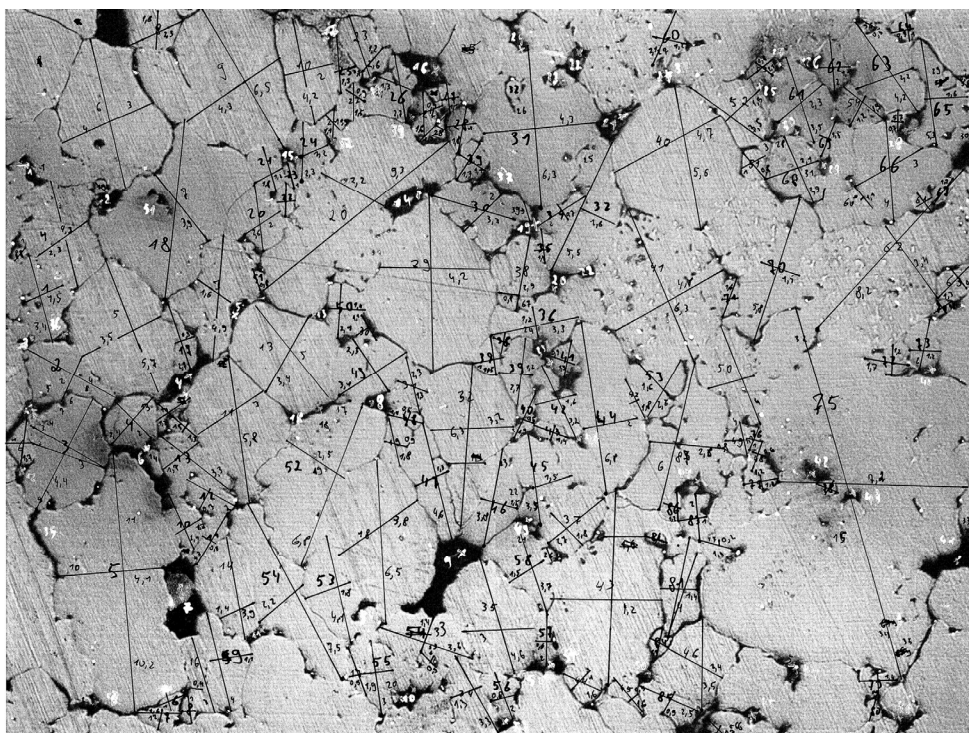


Figure 4.5: Determination of the two semi-axes assuming an ellipsoidal shape of grains. This example shows the manual preparation of the micrograph of figure 4.3a (top).

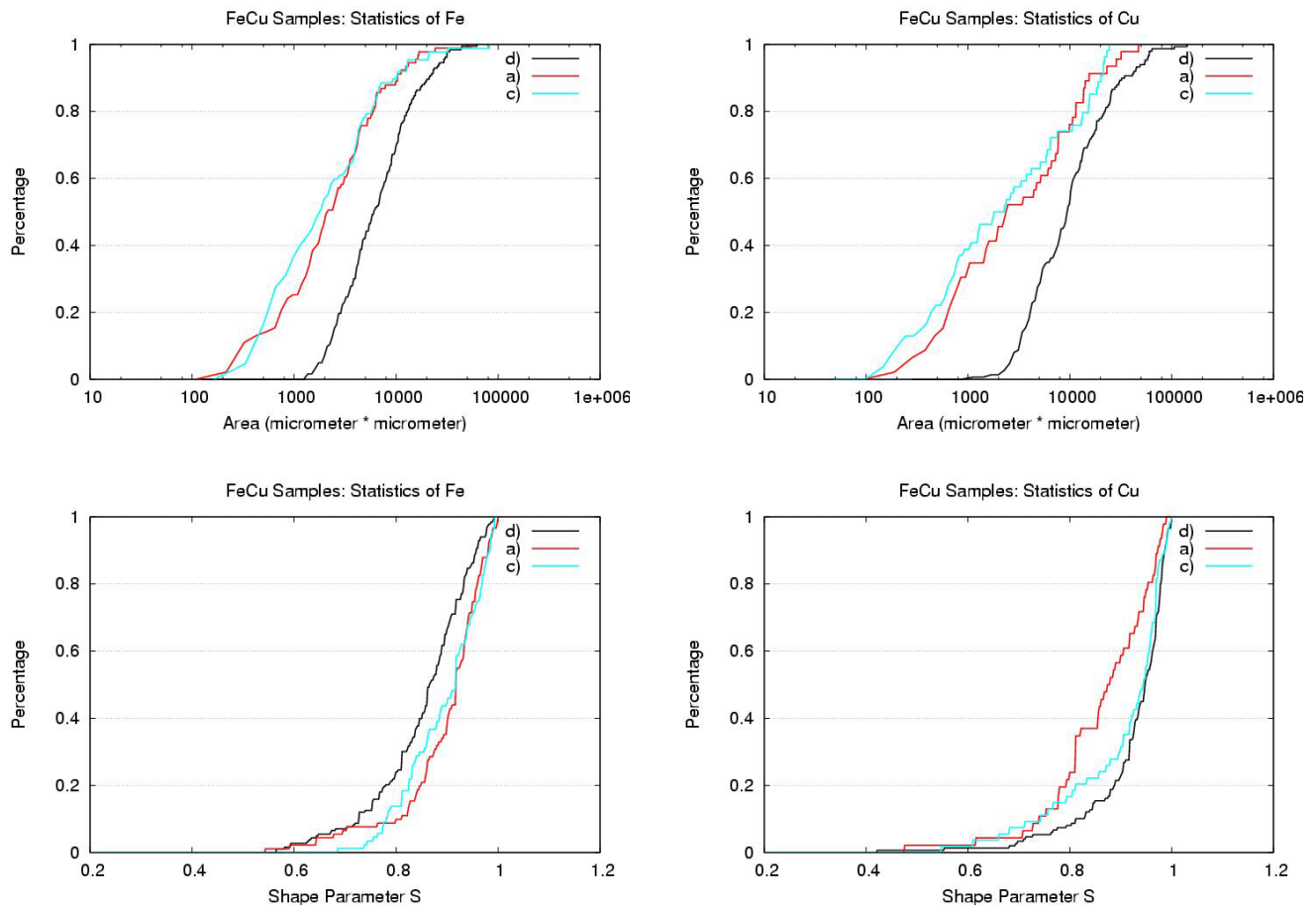


Figure 4.6: Cumulative distribution of grain area and shape value, individually evaluated for Cu and Fe grains. Grains with area smaller than $100 \mu\text{m}^2$ were discarded from statistics. 50 % of counted Fe grains have a size between about $1000 \mu\text{m}^2$ and $50,000 \mu\text{m}^2$ and shape parameters $S > 0.88$. The Cu grains show a similar distribution with slightly larger area values.

4.2 General Remarks on Structure Models

In order to develop useful numerical models of the structure-property relationship of the materials that are studied in this project, as a basic prerequisite, one needs a way of generating “realistic” microstructures of the materials in question. In principle, one could use tomographic techniques to produce data sets that represent a three-dimensional (3-D) structure of a material on the microscale. However, producing 3-D tomographic images of materials is very expensive and generally their resolution as well as the number of measured grains is still poor. Typically, the resolution in 3-D tomographic

images is limited to a voxel edge-length of a few μm which is not sufficient to resolve grain boundaries that are usually only a few nanometers in size.

A different way of producing microstructures directly from a material sample is the use of two-dimensional (2-D) polished micrograph sections generated by chemical etching of materials' surfaces. In essence, one could use these micrographs as a basis for generating a connected mesh that subsequently could be used in a numerical finite element analysis. However, such a micrograph section is just *one* two-dimensional (2-D) sample of the real microstructure in 3-D; thus, the value of its explicit rendering in 2-D is very questionable. Hence, we propose a scheme based on a statistical characterization of the grains on the microscale in terms of the distribution of the grain areas A and the grain perimeters P in order to reproduce these statistical properties in a numerical 3-D model.

In the following several details of this procedure are discussed and the results on exemplary micrograph sections are shown that demonstrate the employed method for generating granular structures in 3-D.

4.3 Technical and Algorithmic Details of POLYGRAIN

The idea of the statistical approach implemented in the tool POLYGRAIN is based on the approximation of the microstructure of sintered materials as a polyhedral cell complex. This is the case in very good approximation for e.g. densely sintered ceramics for which the software was originally developed. Consequently, we use power diagrams – one well studied generalization of the Voronoi diagrams – to model these polyhedral cell complexes. Figure 4.7 shows schematically the applied procedure for generating microstructures from experimental micrographs.

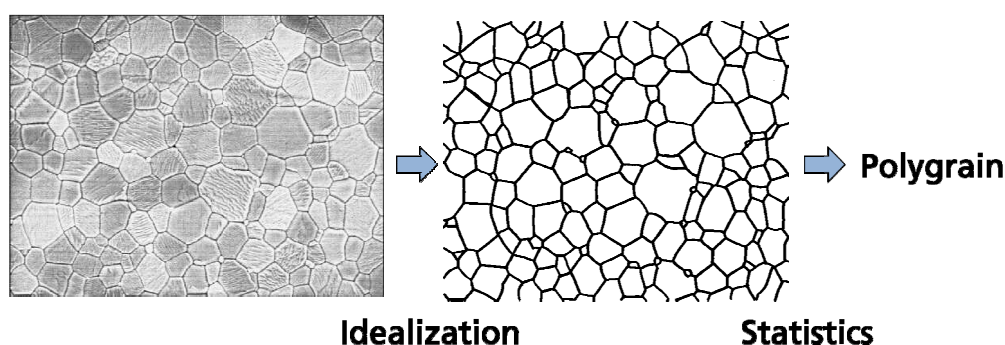


Figure 4.7: Scheme of using POLYGRAIN. The input is the statistical data extracted from the experimental micrograph. Usually, this requires very elaborate pre-processing by hand to ensure an ideal contrast between grain boundaries (black) and grain areas (white) that can be processed by standard pattern recognition software.

Using the experimental micrograph one extracts the statistical information on the grains which usually needs a very laborious preparation by hand. Processing the micrographs directly using commercial software usually results in a very bad contrast in the final digitalized image which again requires further preparation by hand. Figure 4.8 shows an example for the result of a fully automatic digitalization which requires further manual processing due to contrast problems. Therefore, the experimental micrographs are traced by hand so as to ensure an ideal contrast between the grain boundaries and the grains and voids, respectively. Using such an image, the statistical information on the grains' perimeter and area can be automatically extracted by pattern recognition software. In our case, we use KS300 from ZEISS.

For the numerical representation of a polyhedral cell complex, we choose the power diagram (PD) which contains the Voronoi diagram as a special case. The PD extends the Voronoi diagram by adding a scalar weight to each generator point. For PDs efficient worst-case optimal algorithms are available in 2-D and 3-D where the computational efforts are $O(n \log n)$ and $O(n^2)$, respectively.

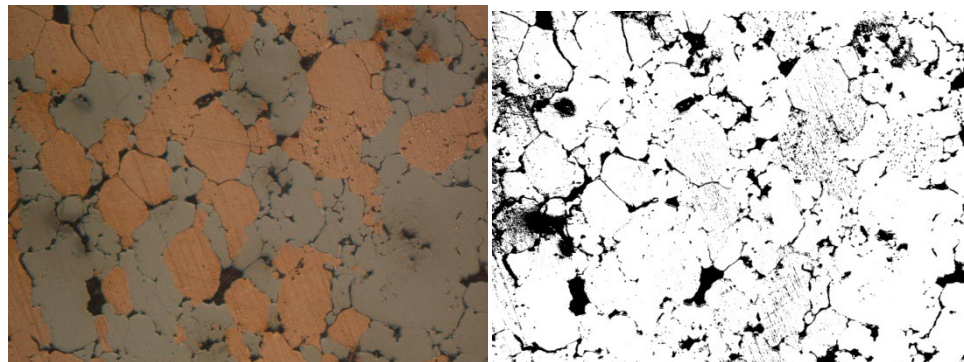


Figure 4.8: Example for an insufficient automatic digitalization of a micrograph using the software KS300 from ZEISS. Left: original micrograph. Right: automatically digitalized image.

The basic idea of our procedure to generate polycrystalline structures is to compare all cells (typically at least ≈ 10000) inside a cube of a given PD in 3-D with the 2-D experimental data. We perform this comparison for each coordinate axis by generating a set of parallel, equidistant 2-D slices through the cube and perpendicular to the respective axis, cf. figure 4.9. For each 2-D slice, the grains' area sizes A are calculated and combined into one histogram. The same is done with perimeter P . Next, we compare the calculated histograms with the experimental histograms. This is done by calculating the first k apparent central moments of the area distribution A_i and perimeter distribution P_i in both cases.

As the experimental distribution is not Gaussian distributed, $k > 2$ should be chosen. Finally, we define a single figure of merit q of conformity:

$$q = \sum_{i=1}^k \left(P_i - P_i^{\text{exp}} \right)^2 / P_i^{\text{exp}} + \left(A_i - A_i^{\text{exp}} \right)^2 / A_i^{\text{exp}}.$$

To derive our model, we start with a Voronoi diagram by choosing Poisson distributed generator points and initializing all weights to zero. The quality number q is calculated from this initial PD. Using a reverse Monte Carlo scheme, we then choose at random one generator point, modify its position, respectively its weight randomly, and check q again. If q has decreased, the move is accepted, otherwise it is rejected. The modification of generator points is continued until q has reached a given threshold, typically 10^{-1} .

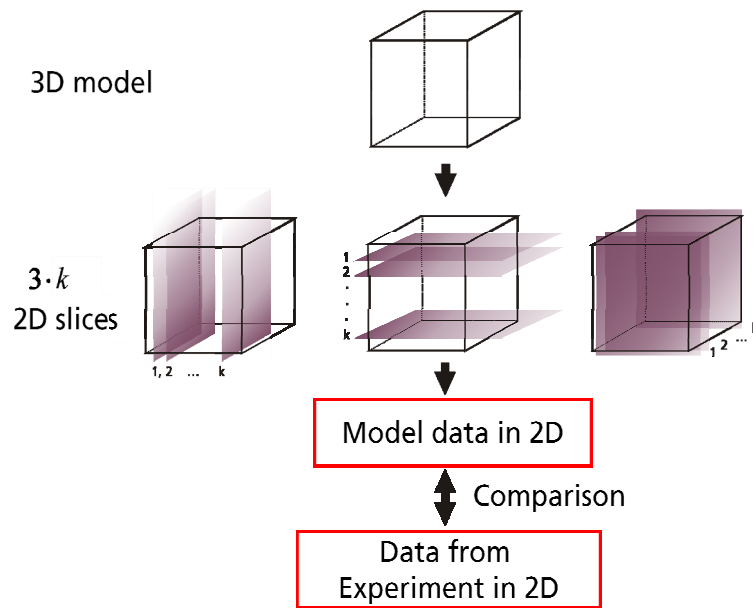


Figure 4.9: Scheme of the generation of PD diagrams in 3-D which are compared with experiment via 2-D statistical data.

If $q = 0$ is reached, the first k central moments of the experimental distributions agree completely with the model. We typically use $n_G = 10,000$ generator points and $n_s = 2000$ slices for each one of the coordinate axes at each optimization step. The number n_s is chosen large enough, such that q is in essence independent of n_s . Note, that the optimization algorithm scales as $O(n_G^{4/3} \log n_G)$ under the reasonable assumption that n_s is chosen as $n_s \sim n_G^{1/3}$.

4.4 Further Developments of POLYGRAIN

After having generated the geometry of the microstructures in the experiment, the obtained data can be meshed using any appropriate meshing tool. However, due to possible very small edges present in the resulting geometric 3-D structures, one occasionally runs into problems in a subsequent FE analysis. Short edges lead to a small time step during a simulation run and might subsequently move the system into a deadlock situation. Thus, extra effort was put into an attempt of avoiding this problem via a special optimization scheme which simply looks for the shortest edges in the calculated diagram and tries to remove them by appropriately moving the connected generator points within the boundaries of a sphere that encloses the shortest edge. Several tests of this procedure were done, e.g. by removing generator points only locally and then re-optimizing the whole PD.

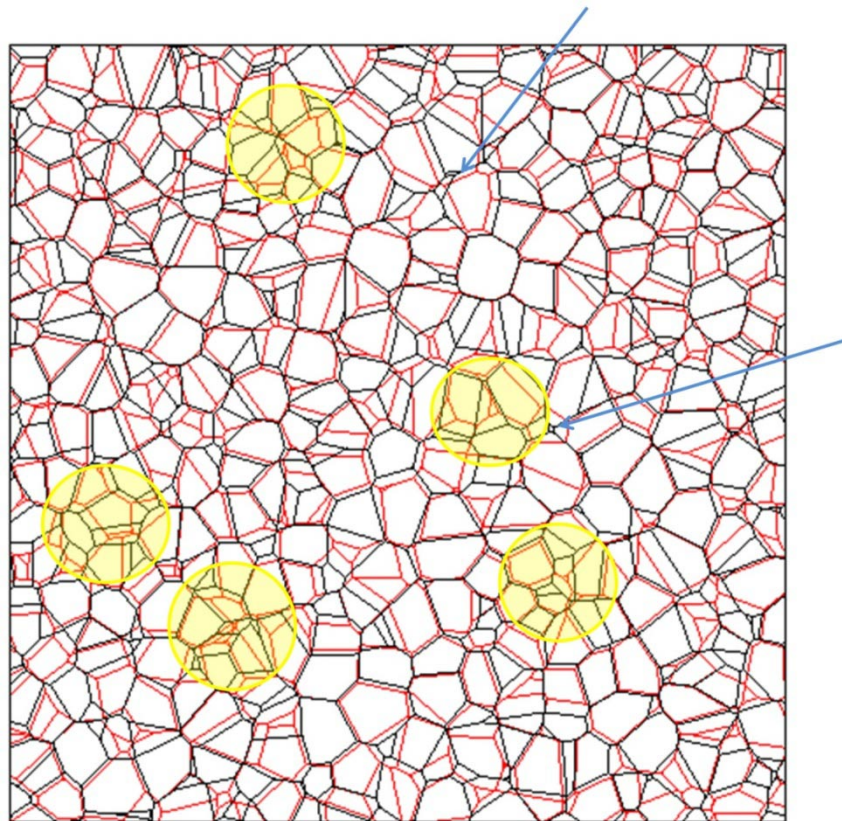


Figure 4.10: Heuristic removal of small edges visualized in a 2-D slice of a 3-D power diagram. Red: original PD in 3-D. Black: result of the optimization within several disjoint boundaries of the PD. Albeit the optimization of critical, i.e. small edges, is restricted to the volume indicated by circles, the removal of short edges here may result in newly generated even shorter edges of grains far away from this area in the 3-D diagram. An example is indicated by the blue arrow. This happens in a vastly non-controllable way.

However, it turns out that the removal of small edges in some areas of the diagram results in elongating other edges at distant areas of the PD, not necessarily directly connected to the generator points within the chosen boundaries of the sphere.

As a result, there only seems to be a heuristic way of reducing the number of small edges by repeated optimizations starting from the same diagram and then choosing the one with the best relative result. As an example of the problems connected with this issue, we show in figure 4.10 the result (black) of optimizing an initial diagram (red) in this heuristic way.

Note that the optimization is done with the full 3-D structure before meshing the geometry. Hence, the two PDs in figure 4.10 just represent single slices of the total PD which is generated and optimized in 3-D.

The application of POLYGRAIN to the FeCu samples shown in figures 4.3 is illustrated below. In figure 4.10, we show the progress in the generation of PDs in a 2-D slice at the initial state and after 100,000 reverse Monte Carlo steps, pertaining to the statistics obtained from the micrograph. As the figure of merit q on average has only decreased by about 20 % down to $q \sim 3.9$ after 100,000 Monte Carlo steps, the PD is has not converged to the desired value. However, the state after 100,000 steps is much closer to the desired distribution than the initial guess.

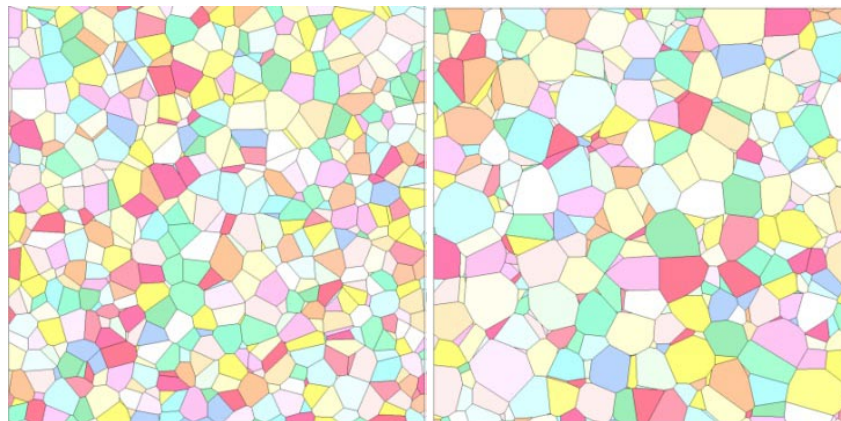


Figure 4.10: Progress of generating PDs for the micrograph of figure 4.3. Left: initial PD. Right: PD after 100,000 reverse Monte Carlo steps, which gradually approaches the distribution in figure 4.4 with many large and very few smaller grains.

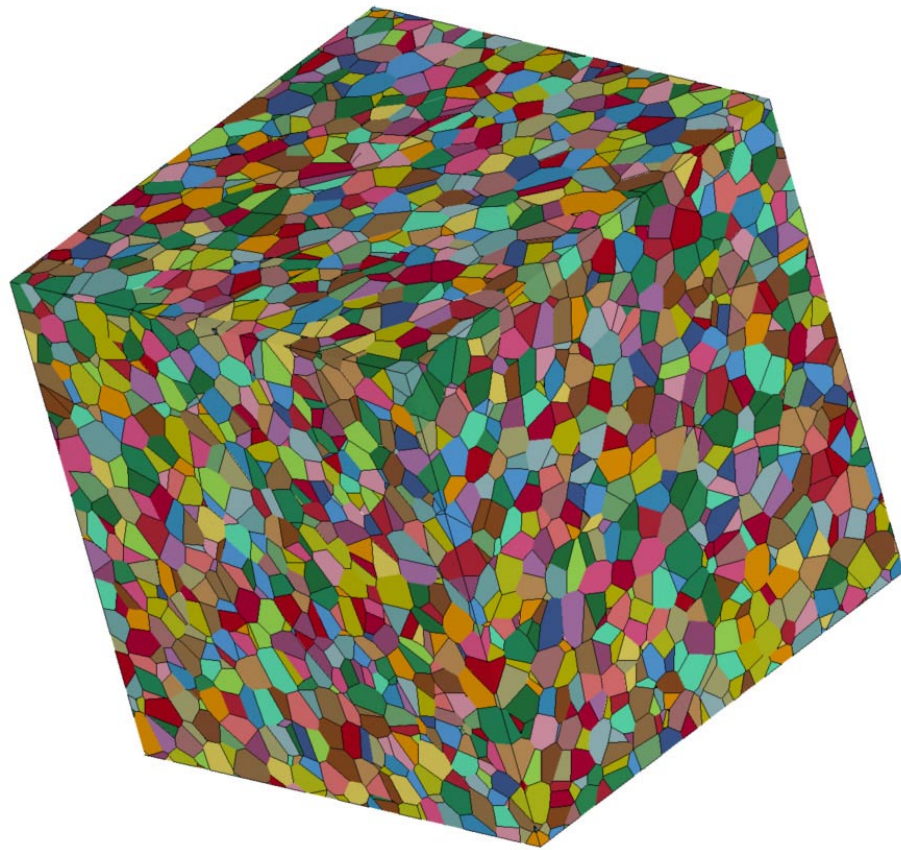


Figure 4.11: Full view of resultant 3-D structure where slice shown in figure 4.10 (right) has been extracted from.

Given a converged grain distribution, the further application of POLYGRAIN will proceed as follows. Under the assumption, that all material constituents obey the same statistical distributions, the specification of the material type of each grain is done randomly. The known mass fractions of materials provide a boundary condition for the random distribution process. A further boundary condition is the porosity of the material. As the initial POLYGRAIN model fills the space entirely with grains, some grains have to be interpreted as pores and will then be deleted from the model. In order to reach the specified porosity, the random assignment of material types to grains is done in order of decreasing grain size. This way, the remaining grains of small size are interpreted as pores and removed from the model.

4.5 Development of a Voxel Based Method

Motivated by the limited applicability of POLYGRAIN for the materials under consideration, a voxel based method has been developed at EMI. The concept applied in this generator is shortly described in the following.

In a first step, a specified number of solid spheres are randomly placed in a cubic box of defined edge length. The spheres can be assigned different material identities and the size of the spheres follows a distribution, which can be individually specified for each material.

In the second step, the spheres are moved to positions with minimum overlap between the spheres. This is achieved by explicit time integration of the equations of motion for all spheres. The motion occurs under mutually repulsive forces according to an inverse quadratic law

$$F_{ij} = \frac{R_i R_j}{d_{ij}^2}$$

where R denotes sphere radii and d is the distance between two spheres i and j . A similar force law is applied between the box walls and the spheres. In addition a velocity proportional damping force is assigned to each sphere. The time integration of the equation of motion then renders equilibrium distributions with a couple of 1000 time steps.

The third step is a growth (or shrinking) process of the spheres, which is carried out in order to adjust the porosity. Within this step, the sphere volumes are mapped to a hexahedral grid of desired resolution. Empty grid cells are identified as part of pores and grid cells inside spheres are part of grains. Regions which are overlapped by two or more spheres are re-assigned a unique material depending on their distances to the different sphere centers. In the iteration process, an enlargement factor is assigned to all spheres, which is changed until the porosity of the resulting voxel model reaches a desired value.

The following figures 4.12 to 4.14 show an equilibrium distribution of 1000 spheres and the resulting material distributions in a 100^3 hexahedral grid. The example contains two materials of slightly different densities (such as Cu and Fe) with mass fractions of 0.5 each. Original sphere sizes are for both constituents in the range 1 to 10 length units. The porosity is 5 %.

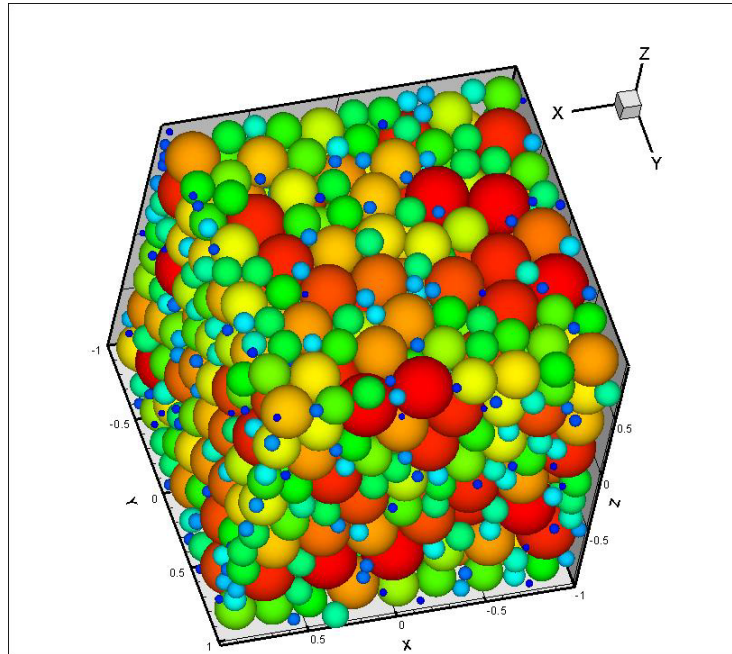


Figure 4.12: Example of an initial sphere distribution as used in a voxel based generator. Color indicates sphere size.

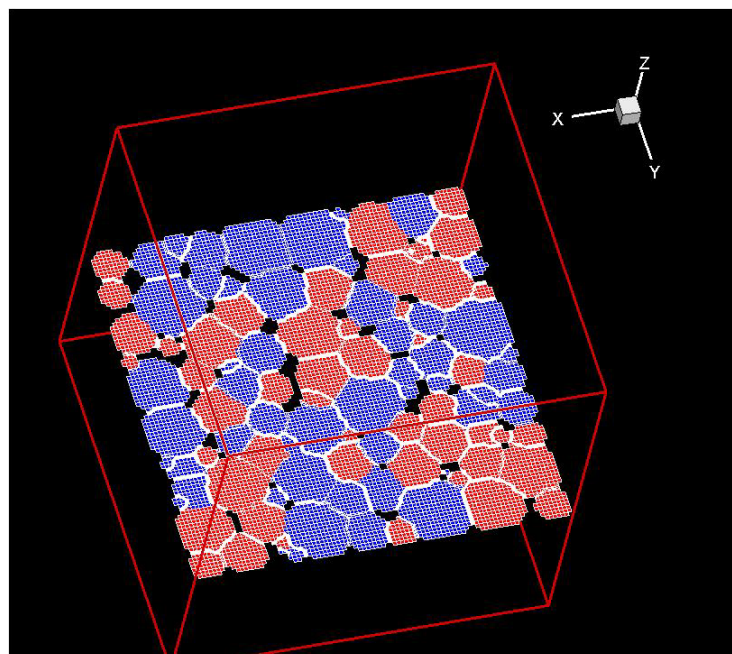


Figure 4.13: Example of a cut section from a grain distribution derived from above sphere distribution. Color indicates material type.

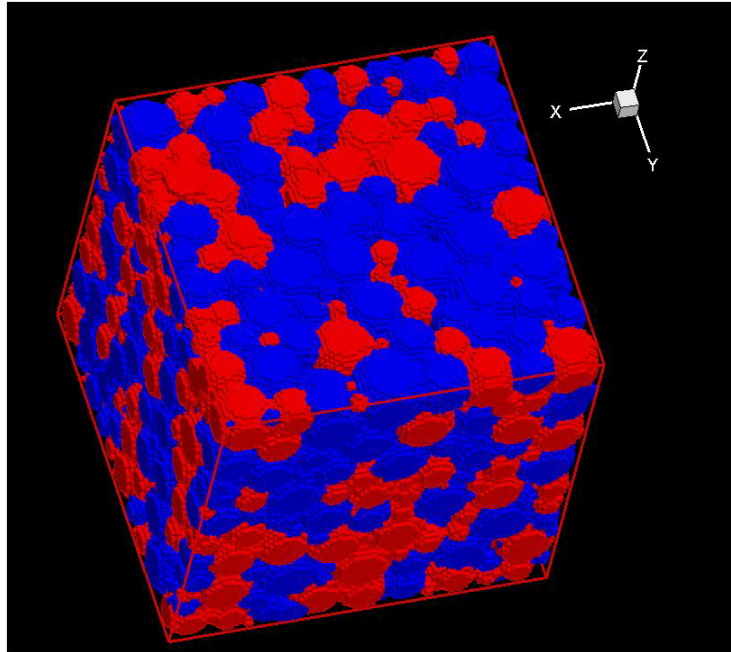


Figure 4.14: Full 3-D view of the grain distribution. Color indicates material type.

4.6 Application of GEODICT

At Fraunhofer ITWM in Kaiserslautern, the software GEODICT, [3], has been developed for a number of years and has since then evolved from an in-house code to a commercial product. It has been applied to generate virtual microstructures of woven and nonwoven fabrics, ceramics, Layered Media and other materials. The microstructures are used for the determination of material properties such as strength, thermal conductivity, filtration etc. The strong point of the GEODICT software is the possibility to identify characteristic properties from two-dimensional (cut) images and to generate representative three-dimensional models on that basis. The technique used is a voxel based representation, meaning that the volume of interest is subdivided in a large number of cubes or cuboids (so-called voxels) and the material information is attached to each single voxel. A number of geometrical objects (different geometrical shapes are possible, e.g. spheres, ellipsoids etc.) are generated in order to fill the volume. Which objects are required and how these objects are placed into the volume determines how well the virtual microstructure represents the original material.

On the basis of the resulting voxel representation, tetrahedral meshes can be generated with GEODICT. In the GEODICT meshes, grain boundaries are resolved with a fine but step-wise approximation, as the meshing is always based on the underlying voxel representation.

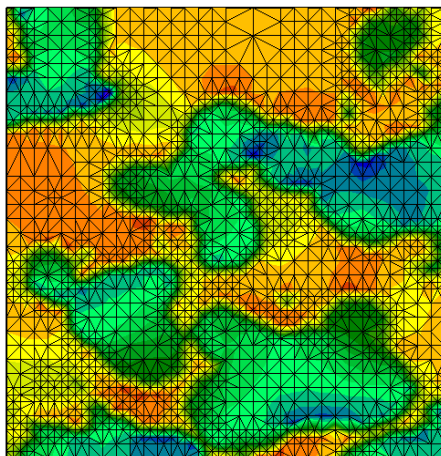


Figure 4.15: Example of GEODICT mesh with adapted resolution.

In order to test the applicability of GEODICT for the materials of interest, the two micrographs shown in figure 4.16 were processed by ITWM. These micrographs are obtained from a FeCu sample. The second picture is a higher resolution cutout of the first picture (enlargements were 8 and 20, which corresponds to a size of about 0.6 mm x 0.9 mm, the higher resolution is about 0.24 mm x 0.36 mm).

It was the goal to generate an artificial volume of about 10 x 10 x 10 grains, corresponding to 0.5 x 0.5 x 0.5 mm. The voxel representation produced by GEODICT (resolution 300 x 300 x 300 voxels) is shown in figure 4.16 below. The porosity in that virtual sample is 5.74 %. The similarity between the grains in the virtual sample and the real shapes can be recognized. The grain boundaries, particularly those of iron, look smoother than in the original. However, given the possible resolution of a FE simulation, it is unrealistic to try to resolve that level of detail. Note also, that the virtual sample is periodic at all boundaries.

Subsequently, the voxel data were used to generate a tetrahedral mesh of the volume. In order to obtain a useful grid resolution a coarsened voxel representation was generated with 100 x 100 x 100 voxels, which resulted in a porosity of 4.15 %. A slice of the resulting tetrahedral mesh is depicted in figure 4.17. As the enlargement shows, all grain boundaries are represented in a step-wise approximation. For the envisaged application of interface elements to represent grain boundary failure in the FE simulation, this step-wise representation is a major disadvantage, as crack paths are unrealistic and cracks are forced to change the cracking mode frequently (from mode 1 tensile crack to mode 2 shear crack). In addition, a high resolution would be needed at the grain boundaries in order to accurately represent the geometrical shape of the grains.

However, apart from the tetrahedral mesh generation, the voxel data can be easily used to generate hexahedral meshes. Such meshes, generated from the structure shown above, are used in the simulation with LS-DYNA (chapter 6).

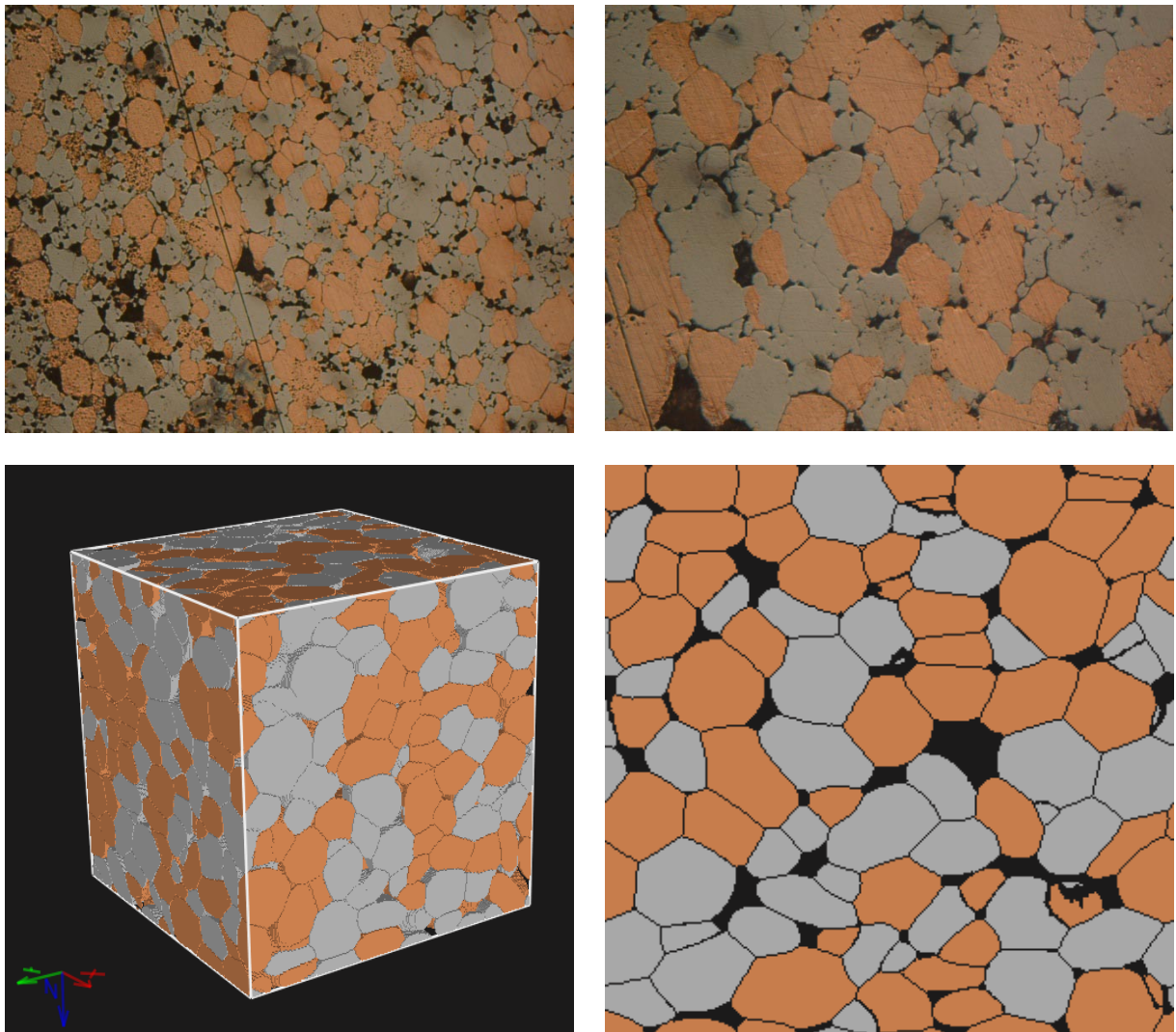


Figure 4.16: Original micrographs of a FeCu sample in two different enlargements (above) and virtual sample created with GEODICT in a 2-D cut and as full representative volume element (below). GEODICT pictures are courtesy of Fraunhofer ITWM.

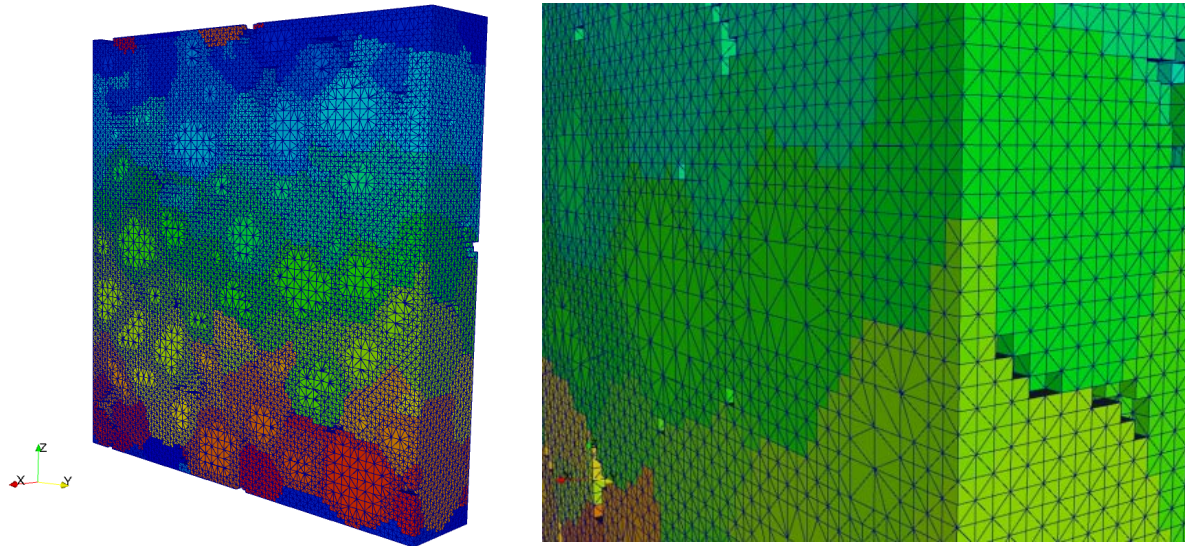


Figure 4.17: Mesh produced by GEODICT from coarsened voxel representation. Left: part of entire mesh. Right: enlargement. Courtesy of Fraunhofer ITWM.

4.7 Application of SIMPLEWARE

In order to overcome the drawbacks in the tetrahedral meshes generated by GEODICT, another software developer, Simpleware Ltd. in Exeter, UK, was contacted. They develop and distribute the software SIMPLEWARE, [4], which is especially designed for the generation of tetrahedral meshes from 3-D data sets such as (Micro-) Computer-Tomography. With this software, it is not possible to generate 3-D data from single 2-D cuts. However, the voxel representation generated by GEODICT or other structure generators can be used to provide the 3-D data input. Different data sets were sent to Simpleware Ltd. in order to explore the mesh generation capabilities.

The first data set was the original ASCII output generated by GEODICT for the high-resolution (300^3 voxel) representation. In that format, all grain boundaries appeared as **marked voxels**. As the pictures below show, the software is able to nicely mesh the structure while smoothing the original stepwise contours.

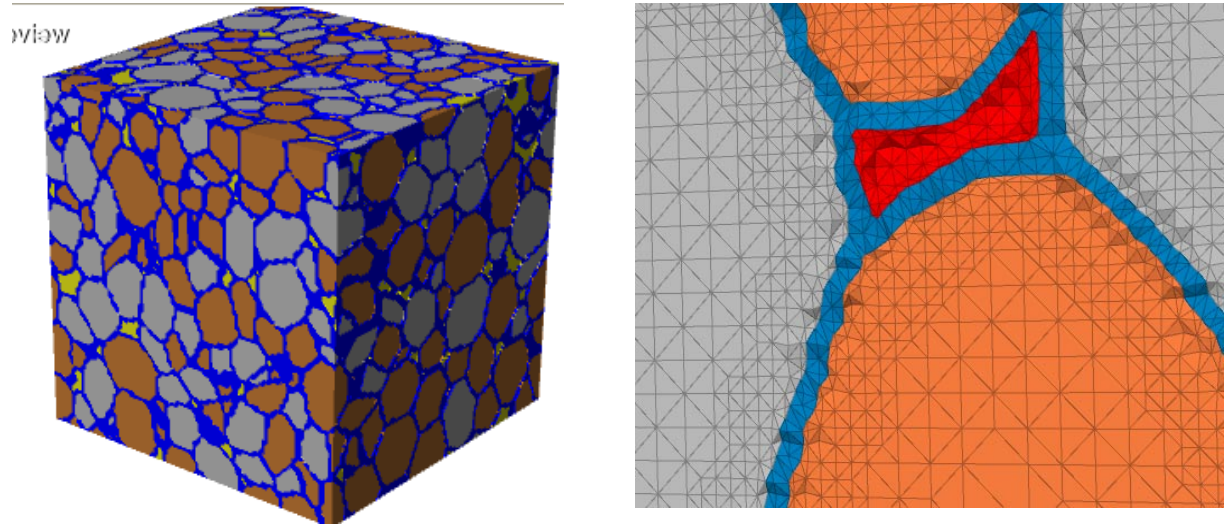


Figure 4.18: Grain distribution and enlarged view of mesh produced by SIMPLEWARE from GEODICT voxel representation with voluminous grain boundaries. Courtesy of Simpleware Ltd.

In order to get a voxel representation without thickened grain boundaries, a different version of a 100^3 voxel representation was generated from the original GEODICT data. In that representation, grains are just distinguished by identification numbers without any voluminous grain boundaries between grains.

The resulting mesh is shown in the following picture. The grain boundaries are nicely resolved and smooth, and the mesh seems well-suited for microstructural FE analysis. Thus, the application of structure generators of the type of GEODICT for the generation of 3-D structures and SIMPLEWARE for the meshing of these structures is a feasible way to generate volumetric representations of the material investigated in this project.

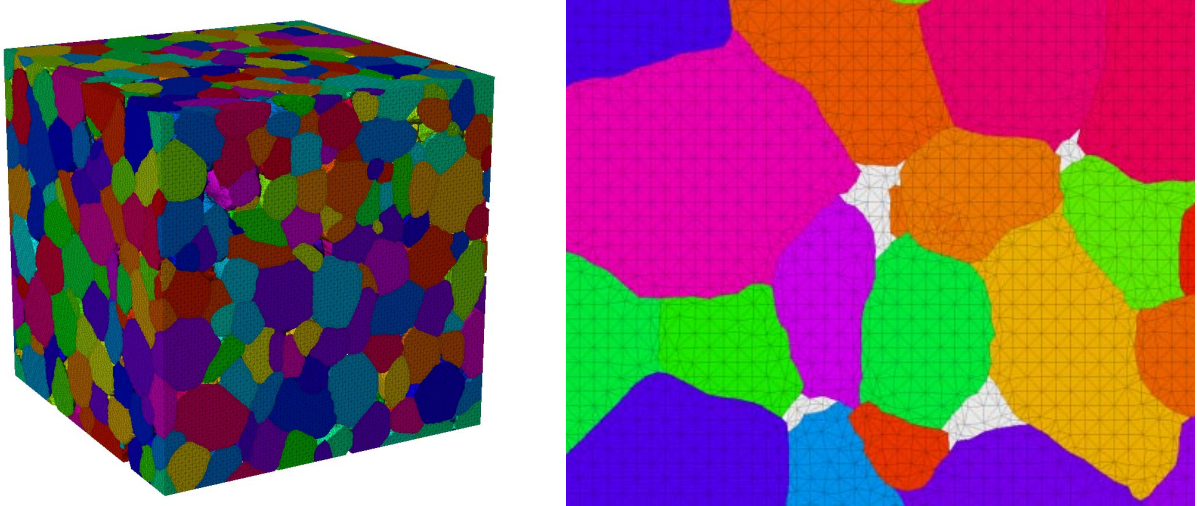


Figure 4.19: Mesh produced by SIMPWARE from GEODICT voxel representation without voluminous grain boundaries. Courtesy of Simpleware Ltd.

4.8 Next Steps

New micrographs will be produced for the different materials of the current lot. These micrographs will be evaluated in order to determine the statistics of grain distributions.

Structure models will then be generated either with POLYGRAIN, the new EMI software as described in chapter 4.5, or with GEODICT, whichever produces the better models. The SIMPWARE software will be used to produce triangular meshes from the voxel models.

5 Advanced Methods for FE Solvers

5.1 Status of MESOFEM

The specialized microstructural FE solver which is being developed within this project is based on the existing FE code MESOFEM developed at EMI. In order to represent the response of microstructures with plane grain respectively grain agglomerate interfaces, the solver has to be capable of handling simplicial triangulations. In general, this means the FE mesh has to consist of tetrahedral volume elements. Interfacial failure is modeled by dynamically inserted triangular interface elements.

The volume element formulation has to be able to account for metal plasticity, i.e. almost isochoric deformation, and has to be suited for highly transient problems, i.e. for explicit time integration. In addition, the formulation has to be efficient enough for the simulation of representative virtual material samples. These requirements limit the choice of element formulations.

In the last two quarterly reports, four alternative volume element formulations were presented and their two-dimensional counterparts partly evaluated. These were:

1. Polynomial pressure projection stabilized formulation proposed by Bochev et al. [5]
2. F-bar method proposed by Souza Neto et al. [6]
3. Average nodal pressure (ANP) formulation proposed by Bonet et al. [7]
4. Diamond elements proposed by Hauret et al. [8]

The first three methods represent different strategies each. (The forth method can be considered as a generalization of the second one.) The formulation proposed by Bochev, called Bochev formulation below, belongs to the class of stabilized mixed methods.

The F-bar formulation is in fact a composite element method since in this method the volumetric part of the deformation gradient of the sub-elements are replaced by the one of a finite macro element. The applicability of the method is limited since the formation of macro elements with few sub-elements is generally not feasible for arbitrary triangulations.

The ANP formulation belongs to the class of nodal integration methods. The “average nodal pressure” calculation is based on the dual volume of the nodes which adds up pro rata from the volumes of the surrounding elements.

Diamond elements are based on the F-bar method and special domain decomposition scheme. This scheme guarantees uniform and complete division of an arbitrary primal triangulation into macro elements consisting of two sub-elements at the cost of the loss of the primal triangulation.

To summarize the cognitions from the last reports: The Bochev formulation was not pursued further since it seemed not readily extendable to nonlinear explicit problems. The ANP method was only considered for comparison since it exhibits significant pressure oscillations near the incompressible limit. The Diamond formulation showed satisfying results in a quasi-static two-dimensional benchmark problem.

5.2 Accomplished Tasks

5.2.1 Volume Element Formulation

Since the Diamond formulation showed promising results in the quasi-static benchmark problem, it was subjected to a dynamic test in two dimensions. The test consists of a generic, i.e. plain strain, Taylor rod impact. The impact was simulated also with the F-bar method applied to a regular triangulation based on divided quads for comparison. The results are shown in Figure 5.1. The F-bar method produces reasonable results. Compared to the F-bar method, the results of the Diamond formulation with regular und irregular meshes show significant pressure oscillations. These oscillations were not apparent in the quasi-static benchmark problem. In addition, the Diamond formulation applied to the irregular mesh exhibits collapsing sub-elements at the boundary. This pathology disqualifies the method.

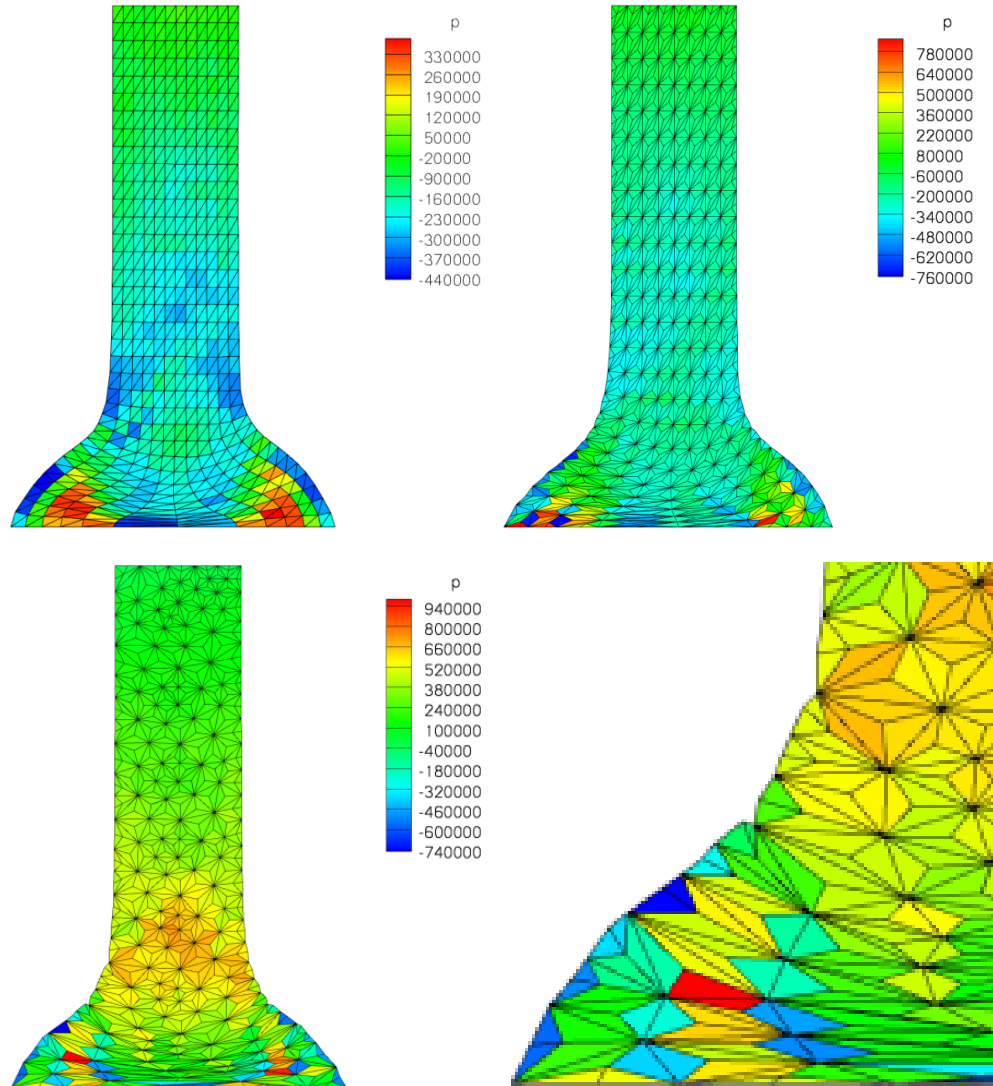


Figure 5.1: Taylor impact. Pressure contour plots [kPa] of the deformed geometry. From top left to down right: F-bar with a regular mesh, Diamond with a regular mesh, Diamond with an irregular mesh, detail of Diamond with an irregular mesh.

In consequence (of the disqualification of the Diamond elements), the Bochev formulation was addressed again. Its principal features were described in the first quarterly report. Reference [5] covers only the implicit solution of the Stokes problem which corresponds to linear elasticity in context of solid mechanics. A first step of extending the method was the formulation of a semi implicit algorithm. The system of discrete displacement equations is decoupled via mass lumping allowing an explicit solution. The system of discrete pressure equations is solved implicitly every time step since lumping of the system matrix would cancel out the desired stabilizing terms. Figure 5.2 shows the results of the P1-

P1 variant (linear displacement and pressure interpolation) of the generic Taylor impact for two different stabilization parameters. The results of the P1-P0 variant (linear displacement and constant pressure interpolation) are not presented because they are well inferior to the ones of the P1-P1 variant.

Since the method was formulated for the totally incompressible case in [5], the choice of the stabilization parameter α for a problem incorporating both compressible (elastic) and incompressible (plastic) behavior is a sensible matter. But the comparison with the results of the F-bar method shows good agreement for $\alpha = 20$.

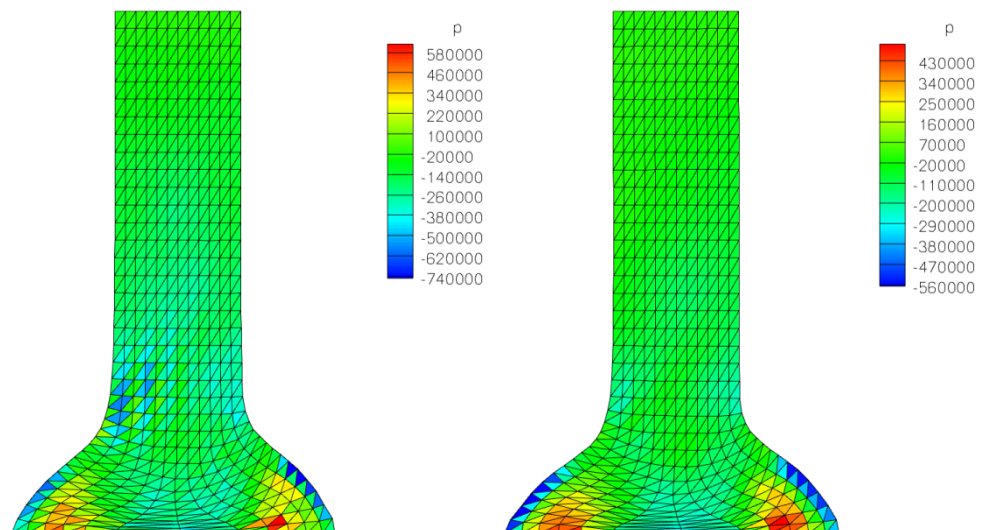


Figure 5.2: Taylor impact. Pressure contour plots [kPa] of the deformed geometry. From left to right: Bochev P1-P1 semi implicit with $\alpha = 1$, Bochev P1-P1 semi implicit with $\alpha = 20$.

The implicit solution of the pressure system is quite inefficient. A further literature research resulted in two stabilized mixed methods with an explicit solution of the decoupled pressure system:

1. Characteristic based split (CBS) formulation proposed by Rojek et al. [9]
2. Finite calculus (FIC) formulation proposed by Oñate et al. [10]

Both above mentioned methods utilize a discrete Laplace operator for stabilization in the pressure equations. Since the stabilization of the Bochev formulation parallels a Laplacian one for certain triangulations (q.v. [11]), a Laplacian stabilization was used as a starting point for a totally explicit mixed method. The time integration is based on a modification of the one presented in [10]. The required stabilization parameter was chosen heuristically (in an ad

hoc manner). A first simulation result of the generic Taylor impact is shown in figure 5.3 which exhibits a good agreement with the one of the F-bar method.

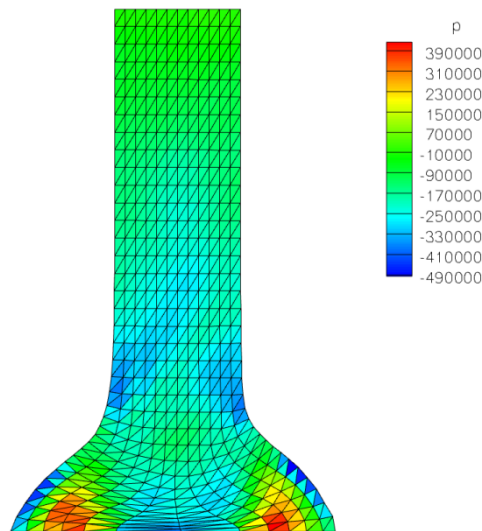


Figure 5.3: Taylor impact. Pressure contour plot [kPa] of the deformed geometry. Mixed formulation with Laplacian stabilization.

5.2.2 Interface Elements

Parallel to the analysis of a volume element formulation, the implementation of the interface elements was begun. The underlying principles were presented in detail in reference [12]. For convenience, the principle is briefly recapitulated in the following.

The response of intact material is governed by volume elements whereas discrete failure is modeled by interface elements. Upon the transgression of a critical traction an interface element is inserted between two adjacent volume elements. During the decohesion process, it determines the traction acting on the adjacent surfaces based on an initial rigid cohesive law (q.v. [13]). If a critical displacement (or crack opening energy) is reached, the cohesive law predicts no further traction. The interface element is then eliminated from the finite element mesh and an internal free surface is left behind.

The kinematic admissible opening forms of an interface element depend on the geometry of the chosen volume and interface elements and the state of the adjacent interfaces. To guarantee convergence, the process zone at a propagating crack tip has to be resolved by at least two interface elements. A brittle material has in general a smaller process zone than a ductile one. Usually, the process zone is significantly smaller than the resolution of the mesh. To circumvent this issue, the cohesive law has to be scaled. For finite

elements bigger than half a process zone, the critical traction has to be reduced and the critical displacement has to be increased while conserving the fracture energy. An applicable scaling law derived from analytical and numerical atomistic calculations is presented in [14].

The current state of implementation differs in two major points from the original reference.

1. The interface elements are of first order to be compatible with first order volume elements.
2. The data structure was simplified as the consideration of element edges could be avoided. Internal facets, which trigger the insertion of the interface elements, are only located at physical (grain or grain agglomerate) interfaces and not between all volume elements.

The result of a two-dimensional pre-notched double cantilever beam (DCB) simulation (shown in Figure 5.4) is presented as proof of principle of the method. As consequence of pulling apart the notched end of the beam the typical stress field forms at the tip of the notch. If the traction between the volume elements adjacent to the notch-tip surpasses the permitted critical traction, an interface element is inserted and the node at the notch-tip is split. This happens the first time between 5 ms and 10 ms in the presented simulation. During the propagation of the crack through the beam this process is repeated. The interface element, the response of which is governed by a cohesive law, prevents the spontaneous release of the new formed interface. Without it, the crack would propagate unregulated, i.e. significantly faster than reasonable, through the beam. In fact, the simulated crack slows down during its propagation. This is particular noticeable at 50 ms, 100 ms, 150 ms and 200 ms.

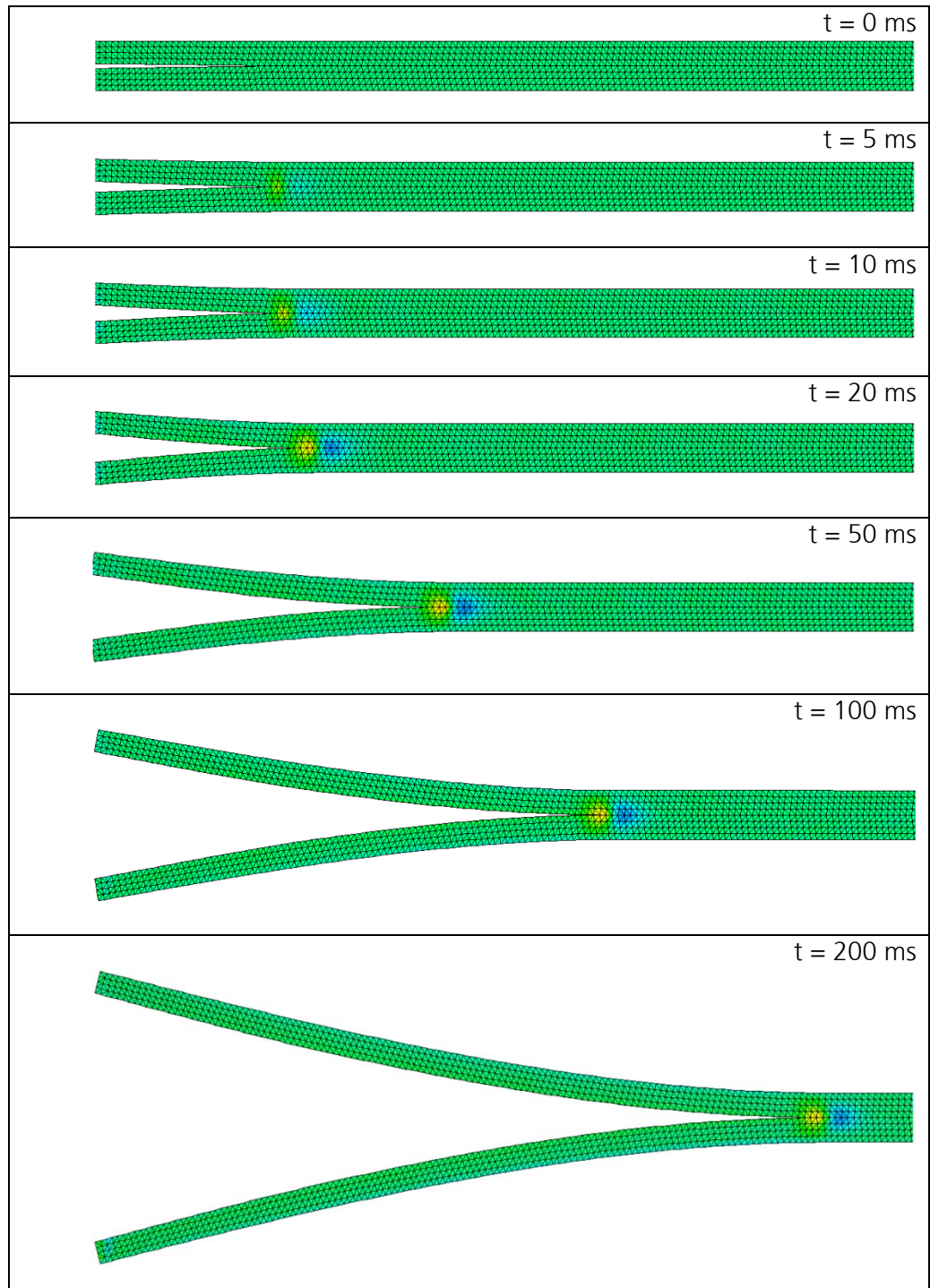


Figure 5.4: Two-dimensional DCB test. Contour plots of the stress normal to the separation plane at different stages of crack propagation.

A three-dimensional demonstration of the method is based on the generic polycrystalline structure shown in Figure 5.5. It consists of 172 grains and measures $3\text{ }\mu\text{m}$ by $1.5\text{ }\mu\text{m}$ by $1.5\text{ }\mu\text{m}$. Both square sides of the volume are pulled apart with 200 m/s each while maintaining lateral confinement to ensure plain wave propagation. The material parameters of the virtual sample are chosen arbitrarily for this demonstrative application. The result of the simulation is presented in Figure 5.6. The results have to be considered as a proof of concept. This is especially true in consequence of the non-smooth boundaries of the volume. Nevertheless, the formation of discrete cracks in a three-dimensional body is demonstrated.

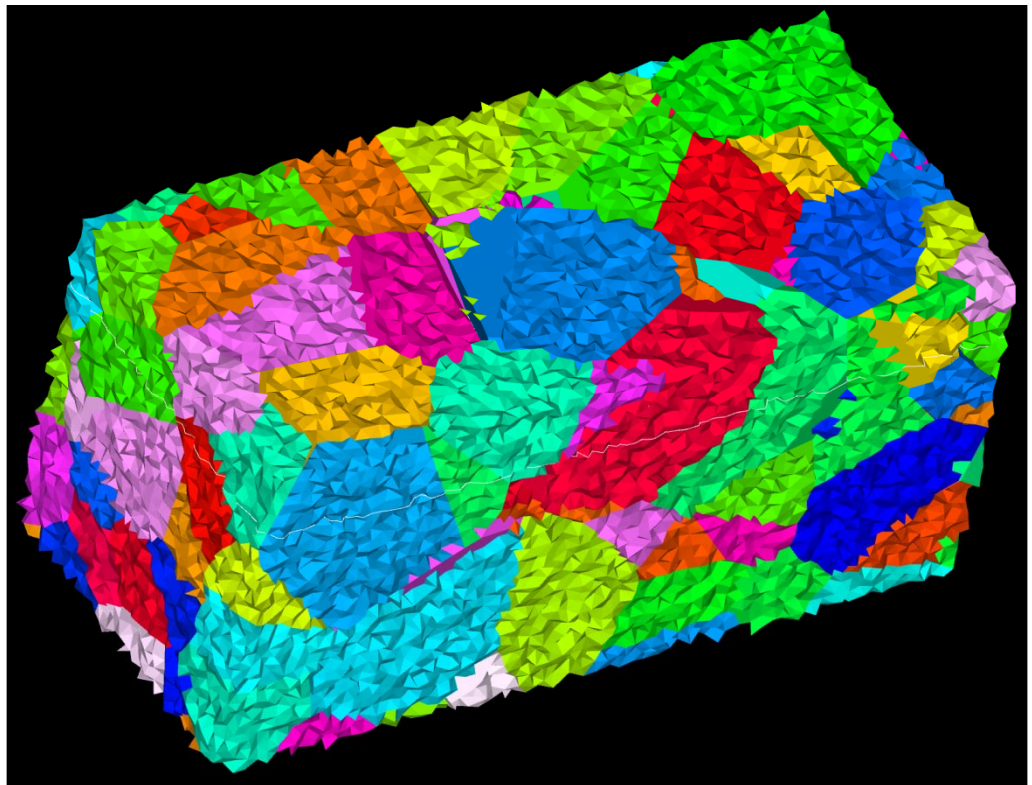


Figure 5.5: Generic polycrystalline structure.

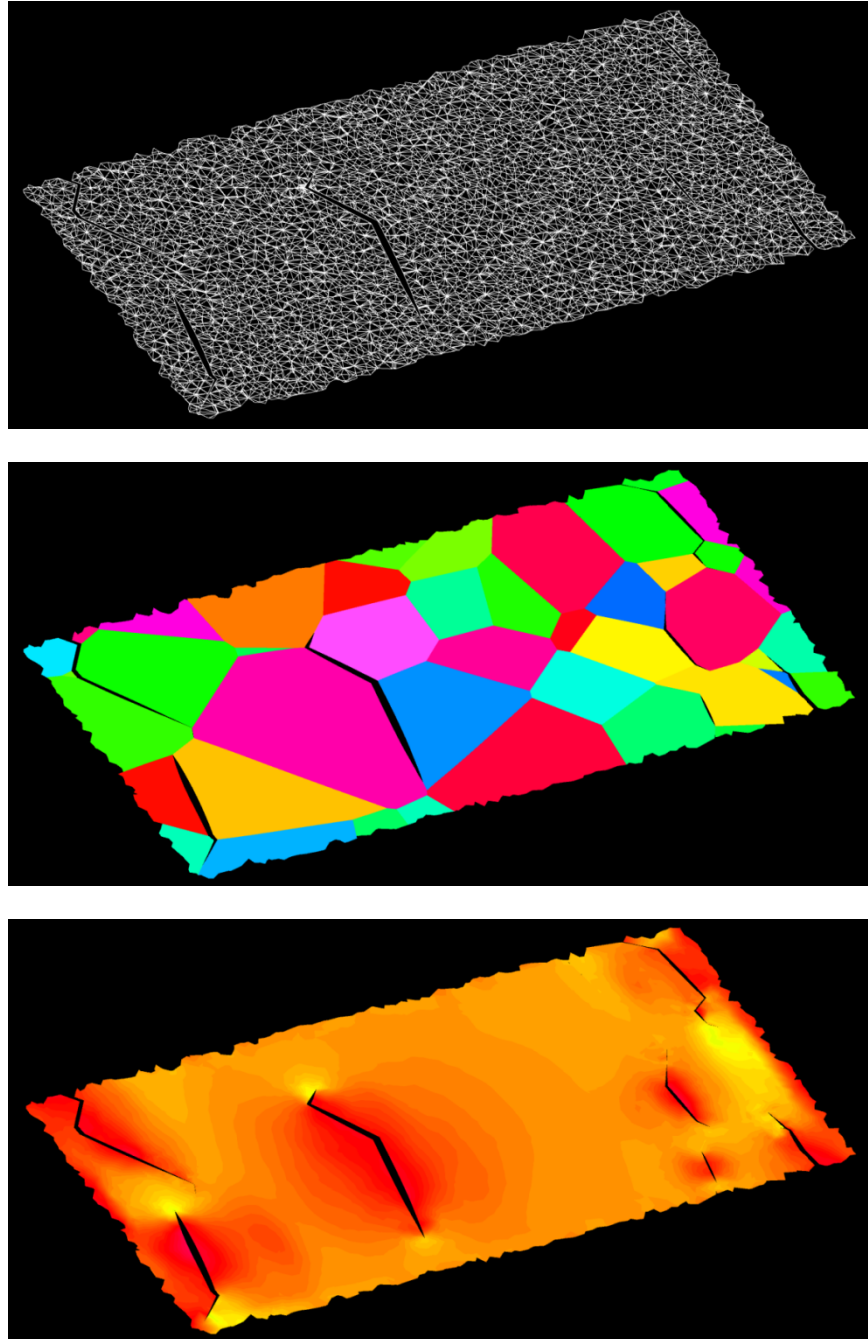


Figure 5.6: Slice through the final state of the generic polycrystalline structure. Top down: projection of the mesh onto the slice plane, visualization of the different grains, contour plot of the pressure.

5.3 Next Steps

The development of the totally explicit volume element formulation will be continued. Hereby, two issues stand out.

1. Sophistication of the stabilizing operator in regard to its influence on wave propagation
2. Automatic determination of the stabilization parameter in dependence of the degree of incompressibility

After the determination of key features of the stabilized volume element formulation the interface elements have to be adapted to guarantee compatibility which is mandatory for the stability of the overall method. This is particularly related to the contribution of the interface elements to the nodal pressure, which was introduced as additional free unknown by the utilization of a mixed volume element formulation. Furthermore, the scaling law for the cohesive law (q.v. [14]) has to be implemented.

6 Alternative Methods and Simulation of Tests

6.1 Requirements and Approach for the Simulation

Pertinent to the available computer power, the simulation of material on the mesoscopic scale is still restricted to small volumes. Hence, only a representative volume element (RVE) is considered to predict the behavior of the grain structure in the material. For an evident calculation it is necessary to determine loading and boundary conditions, which agrees with the state of selected RVEs in the body. The load of the RVE is estimated by measuring the mechanical field quantities in the considered section during a simulation of the whole body. Here, a macroscopic material model is needed which can approximate the mesoscopic behavior of the material as precisely as possible. For the definition of the boundary conditions, you have to keep in mind that the RVE is always surrounded by material. For the illustration of this circumstance, a setup for a flying plate test is depicted in figure 6.1. RVEs in selected locations are marked blue. The impactor induces a shock wave in the target. The boundary conditions of the RVEs depend on the location of RVE in body. For the RVE in the center of the body the wave propagates through the RVE and leaves it at the opposite surface. So the chosen boundary conditions have to prevent a reflection of the wave at the surface of the RVE.

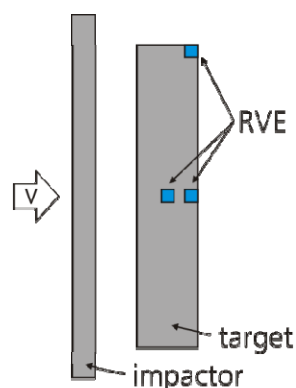


Figure 6.1: Example of a flying plate setup with several RVEs in different positions of the specimen.

Another aspect which has to be regarded is the approximation of the fracture or spallation behavior in the grain material with the RVE. For fragments in the size of the RVE the spallation occurs on the mesoscopic scale and is approximated accurately with the RVE. For bigger fragments which include many RVEs, it is difficult to make a prediction. Depending on the location of

the RVE in fragment, the RVE may either be unfractured or it may show only one full-length crack. These preliminary considerations must be taken into account for estimating the possibilities and limits of mesoscopic simulations with discrete RVEs.

6.2 Direct Simulation with Hexahedral Meshes

In the following, the considered representative volume element (RVE) is approximated with equidistant finite element meshes consisting of hexahedral elements. This type of discretization is also called voxel based mesh. The regular shaped under-integrated elements provide stable behavior during the calculation. The 3-D finite element mesh is developed from micrographs of the considered materials. The RVE is a cube of 0.5 mm edge length which consists of approximately 100 x 100 x 100 elements. The porosity of the RVE is about 4.2 %. For the simulation of the decohesion process, the elements which are located at the interfaces between the grains must be identified. Then another material model with failure is assigned to these boundary elements. The behavior of the introduced boundary material is evaluated and adjusted by comparing the results of the simulations with experimental material tests. The next step is to simulate RVEs under dynamic loadings which occur in spallation experiments like the flying plate test or the Taylor test. This helps to understand the mechanism of fracture and spallation in the RVE. An important aspect here is to estimate boundary conditions for the RVE so that RVEs at different locations in the specimen can be approximated correctly. The finite element solver LS-DYNA is employed for the simulations.

The basic idea of the algorithm is to identify the grains which are neighboring to each finite element node. For this, the grain identification numbers of the bordering finite elements are assigned to the nodes. Then every node is queried for the number of bordering grains. If a node is part of multiple grains, a grain boundary is found. Then the grain identification numbers for related elements are replaced by the id of an interface grain. The idea is illustrated in figure 6.2. The boundary elements are colored grey. The advantage of this algorithm is that all possible connections between two grains are captured. An algorithm which only searches for the interfaces of the elements would not find the red marked connection in figure 6.2. A disadvantage of this approach are bulky grain boundaries which result in a high amount of boundary elements, see figure 6.2b). For an optimized algorithm one grain is excluded from the replacing process. So the introduced interfaces are thinner as depicted in figure 6.2c). Here, the boundary elements of the blue grain are not modified.

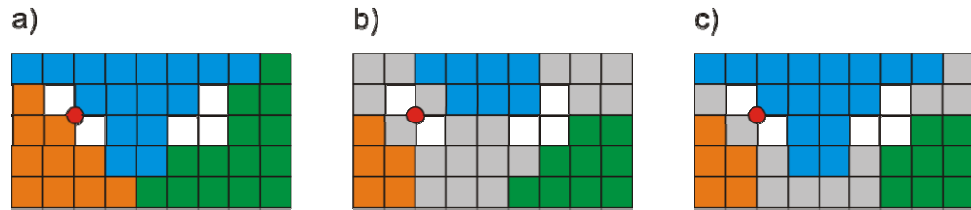


Figure 6.2: Identification of the grain interfaces via element nodes: a) initial mesh, b) after introducing boundary elements, c) optimized algorithm.

The developed algorithm is applied to the cubic mesh of 0.5 mm edge length which is depicted in figure 6.3. It was generated with GEODICT by Fraunhofer Institute ITWM from a micrograph of a FeCu compound. The mesh contains 958,363 elements and 601 grains. After introducing grain interfaces 276,979 elements are replaced.



Figure 6.3: Introduction of grain boundary elements, left side: unmodified mesh with 958,363 elements, right side: mesh after introducing 276,979 boundary elements.

The discretization depicted on the right side of figure 6.3 is used to simulate a specimen of copper. Although the mesh was generated for FeCu, it is applied for Cu because a mesh with the grain structure of Cu is not available yet. The reference material was light sintered with a pressure of 400 MPa and a temperature of 700 °C. An isotropic plasticity model with failure is assumed for the boundary elements. The grains are modeled with isotropic elasticity for impact tests and with isotropic plasticity with fracture for tensile tests. The application of a fracture model for the grains stabilizes the simulation because local discontinuities are avoided by the failure criterion. The usage of the

relative simple material models accounts for a small number of parameters and the interpretability of the associated mechanisms.

6.2.1 Tensile Test

The tensile test is used to determine the quasi-static parameters for the boundary material by comparing the results with experimental data. The parameters are preliminary unknown because the boundary material represents only the cohesion between the grains. The stiffness of the boundary material is assumed equal to the grain material. So the stiffness of the RVE is not modified by the high amount of boundary elements. The simulation is accomplished by a constant strain rate of $\dot{\varepsilon} = 0.003/\text{ms}$ which is applied by surface boundary conditions. Furthermore, a linear distributed initial velocity along the tensile direction is used to avoid accelerations in the first time step. A mass scaling algorithm is applied to extend the time step for the explicit calculation. The application of a contact algorithm between the grains has no effect on the results. The simulation is terminated for $\varepsilon = 0.15$. The cube after failure is depicted in figure 6.4. One may notice a continuous crack running through the whole specimen.



Figure 6.4: Cracked specimen at an elongation $\varepsilon = 0.15/\text{ms}$.

The calculation takes about 15 h by applying 16 CPUs. Here, 25 % of the CPU-time is used for evaluating the cross section force of the specimen which is needed to estimate the tensile stress. The resulting stress-strain curve compared with experimental data is depicted in figure 6.5. In spite of the relative simple approach for the material, its behavior is approximated sufficient. Additionally, the results of an eighth part of the mesh are presented in figure 6.5. Here, a

size effect is obvious, which fits to experimental observations and accounts for the stochastic distribution of weak points in specimen.

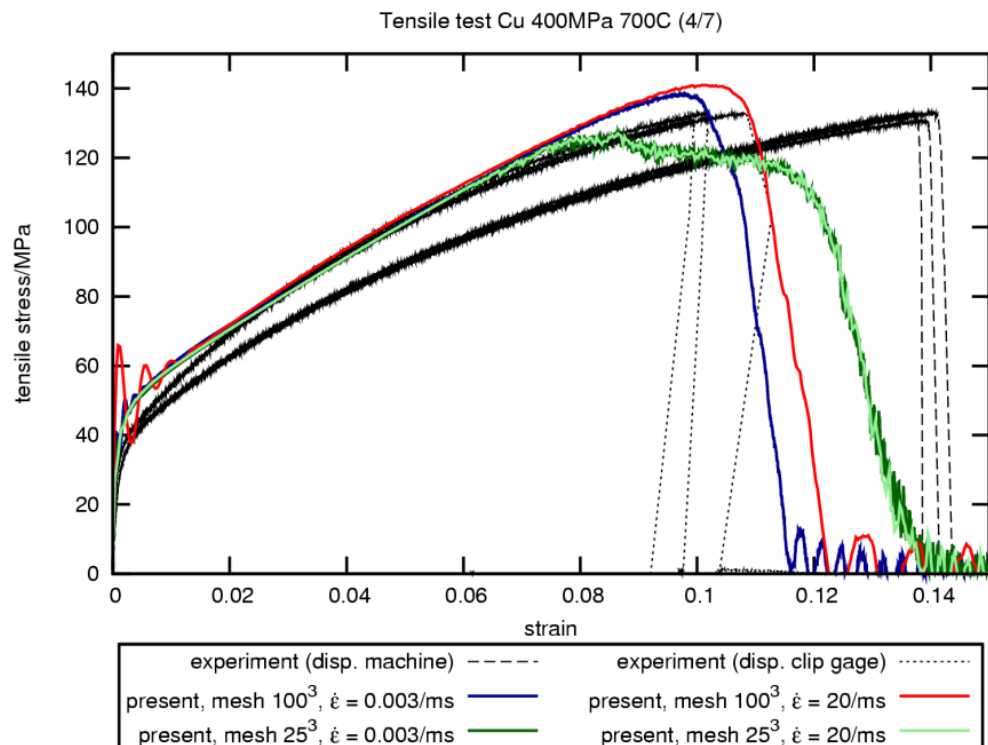


Figure 6.5: Stress-strain curve for the tensile test. The failure behavior depends on the size of the specimen.

Additionally to the quasi-static loading conditions, simulations under a high strain rate of $\dot{\epsilon} = 20/\text{ms}$ are accomplished. Figure 6.5 points out, that the strain rate has no effect on the results of the small mesh with 25^3 elements. But differences are visible for the 100^3 elements mesh. The simulation with $\dot{\epsilon} = 20/\text{ms}$ shows a slightly higher fracture stress and strain. This behavior is also confirmed by the fracture energy of the considered simulations, which can be measured with the amount of failed boundary elements. For the quasi-static example, 10 % of all boundary elements fail whereas this quantity is 12.4 % for the high strain rate loading. An increased amount of failed elements means a larger crack surface and accordingly higher fracture energy. The applied material model does not cover rate dependency. So the rate effect must occur from the grain structure of the RVE. This important conclusion demonstrates the potential of the approach with voxel based meshes and might help to understand the fracture mechanism of the considered light sintered materials.

6.2.2 Impact Test

An impact test is proposed for first dynamic simulations considering wave propagation, fraction and spallation behavior of the light sintered material. The material parameters are assumed with respect to the results of the tensile test.

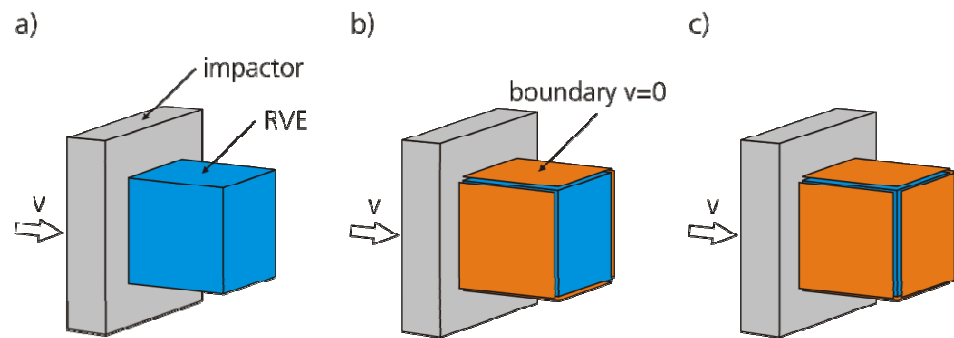


Figure 6.6: System configuration for impact test under different boundary conditions: a) without constraint, b) boundaries at the side surfaces, c) cup-shaped constraints.

Hence, no experimental data for compression is available yet, no failure for compression is assumed. The system is depicted in figure 6.6. Three different setups for boundary conditions are considered. The RVE in figure 6.6a) has no constraints and serves for exploration of the spallation process. In Figure 6.6b), the normal velocities of the side surface are constrained to zero. This represents a RVE at the surface of the target, also see figure 6.1. In figure 6.6c), the normal velocities of all unloaded surfaces are set to zero. The impactor is modeled as rigid body and hits the RVE for a given time between $0.01 \mu\text{s}$ and $0.04 \mu\text{s}$. The velocity of the impactor is constant and varies between 100 m/s and 400 m/s . The time interval of the simulation ends at $t = 1.2 \mu\text{s}$ with a calculation time of approximately 3:30 h. The calculation is restricted to one CPU because of the usage of the ERODING SINGLE SURFACE contact of LS-DYNA. The contact algorithm has a share of approximately 50 % of the CPU time.

The spallation of the unconstraint RVE under an impact of 200 m/s is depicted in figure 6.7. The gray-colored boundary elements are nearly completely destroyed by the impactor. So the fragments conform to the grains of the material.

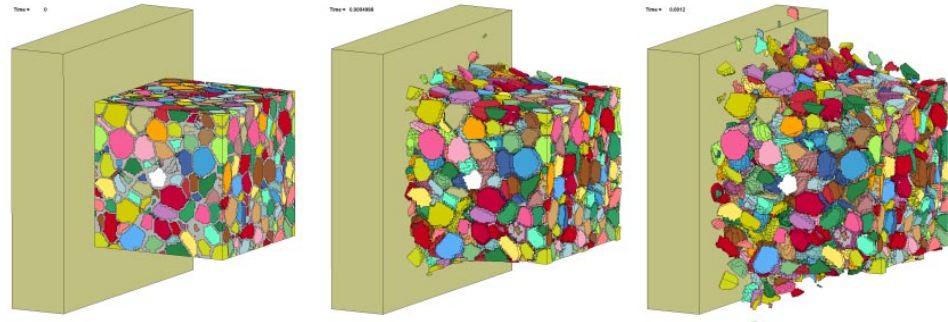


Figure 6.7: Spallation of the unconstrained RVE. Impact with $v = 200$ m/s, impact time $0.02 \mu\text{s}$ at the time steps $t = 0$, $t = 0.35 \mu\text{s}$, $t = 1.15 \mu\text{s}$.

The setup from figure 6.6b) shows another fragmentation behavior. The results of the simulation are given in figure 6.8 for two different time steps. Here, the boundary elements in the left part of the RVE remain partly intact. However, in the right half a crack arises where all boundary elements are eroded. This illustrates that different fracture behaviors can be approximated with voxel meshes by varying the boundary conditions.

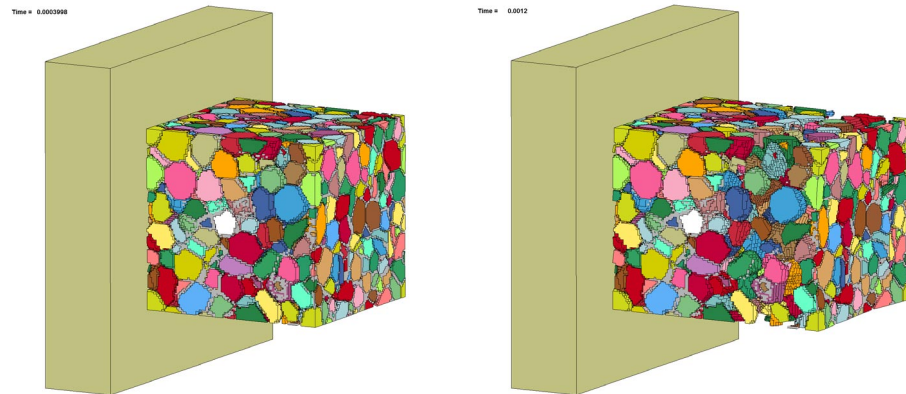


Figure 6.8: Spallation of the unconstrained RVE. Impact with $v = 100$ m/s, impact time $0.04 \mu\text{s}$ at the time steps $t = 0.3 \mu\text{s}$, $t = 1.1 \mu\text{s}$.

In the last setup of figure 6.6, all free surface are constrained. This means that the RVE is pressed into a kind of cup-shaped form. The shock wave propagating through the RVE is reflected as pressure wave at the right boundary. Here the approach differs from a random RVE in center of a body, where the wave is not reflected at the surface. The results of the simulation are given in figure 6.9 for the time steps $0.17 \mu\text{s}$ and $1.1 \mu\text{s}$. For $t = 0.17 \mu\text{s}$, the

wave reaches the right boundary. At this point the amount of failed boundary elements is 34 %. At the time step $t = 1.1 \mu\text{s}$ 95 % of the boundary elements are eroded.

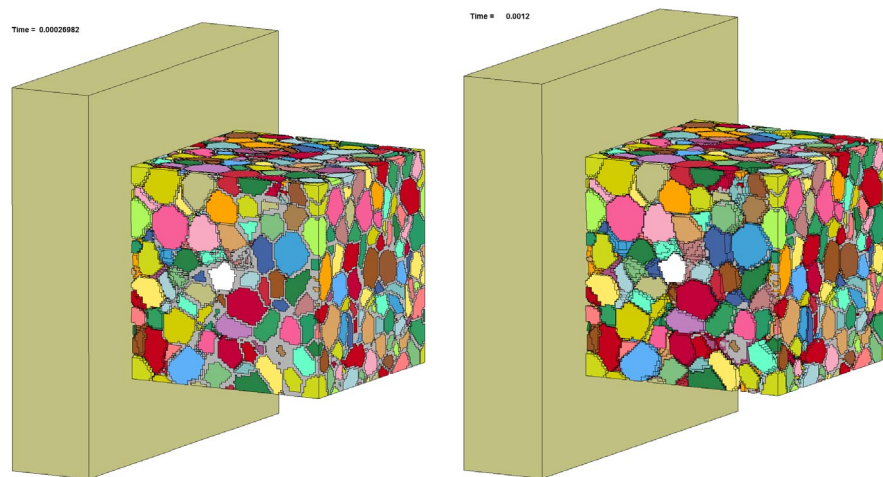


Figure 6.9: Spallation of a RVE with cup-shaped constraints. Impact with $v = 100 \text{ m/s}$, impact time $0.04 \mu\text{s}$ at the time steps $t = 0.17 \mu\text{s}$, $t = 1.1 \mu\text{s}$.

It must be assumed that reflected pressure waves influences the spallation. So, non-reflecting boundary conditions have to be introduced for the simulation of inner body RVEs.

The amount of eroded boundary elements can be measured by monitoring the mass of all boundary elements. The quantity of remaining elements is plotted over time in figure 6.10 for different impact velocities and times under the boundary conditions of figure 6.6a)-c). The number of eroded elements increases for higher impact velocities despite the reduced impact time. The applied boundary condition also influences the failure behavior of the elements. Here, it is interesting that the constraints b) and c) show same eroding behavior for $t < 0.15 \mu\text{s}$. Subsequently, the erosion for constraint type c) slows down. This might result from the pressure wave which is reflected from the surface of the RVE. However, this type of plots might be a helpful criterion to evaluate the fracture behavior of the material

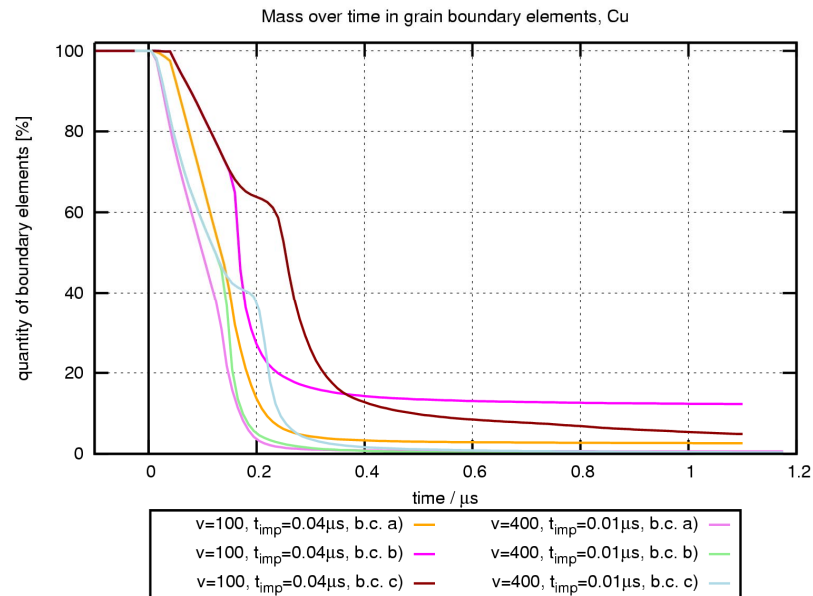


Figure 6.10: Quantity of boundary elements over time for different impact velocities and times under the boundary conditions of Figure 6.6a)-c).

6.3 Preliminary Assessment

The accomplished finite element simulations have shown that voxel based meshes are a possible approach to approximate the mechanical response of grain agglomerates on mesoscopic scale. Commercial finite element codes like LS-DYNA can be used because no special solid or interface element formulations are needed. The interfaces between the grains are modeled by replacing the material model in the elements at the surfaces of the grains. These grains can be identified by a search algorithm. However, the number of boundary elements is large for the presented mesh with 601 grains. This results in a high amount of parasitizing volumes, which properties are hardly assessable. For the simulation of the FeCu specimens, an improved algorithm is necessary which can distinguish between different types of interfaces. Then, a Fe-Fe boundary element gets another material identification than an element for a Fe-Cu or Cu-Cu interface.

The first considered example was a tensile test which serves for the evaluation of the material parameters for the boundary elements. The simulations indicate that a isotropic plastic failure model obtains good agreements with experimental data. For a better adjustment of the interface material, a comparison with further experiments under other loading conditions like

compression or shear is proposed. Another interesting aspect is to examine size effects of the material. Furthermore, specimens of Fe and FeCu have to be simulated.

In a second example, the behavior of the RVE under high dynamic loading conditions was simulated. A shock wave which was induced by an impactor hits the specimen. The impact velocity and time were varied. Another aspect of the example was to examine the influence of different boundary conditions to fracture behavior of the material. This is important to predict fracture behavior in special points of the macroscopic structure. Here further efforts are needed to apply the results of macroscopic simulations as inputs for the mesoscopic calculation. The outcome may be also useful for simulations with tetrahedral elements.

The used finite element solver LS-DYNA proved to be appropriate for accomplished simulations. Anyway, the applicability of other hydrocodes like ANSYS AUTODYN or in-house code SOPHIA should be tested. The runtime of the calculation is acceptable. The quasi-static tensile test takes about 15 h while the calculation of the impact test is finished after 3:30 h. Here a parallelized version of the used ERODING SURFACE CONTACT would help to reduce the runtime significantly. The proposed finite element mesh consists of approximately 10^6 elements. RVEs with more elements are badly manageable for pre-/post processing.

One obvious disadvantage of the presented approach is that the boundary layer of the grains is approximated inexactly, which results from the finite dimensions of the elements in the boundary. Here, the discretization with tetrahedral elements connected by dynamic introduced interfaces would provide a better approximation of the mesoscopic structure.

7 References

- [1] A. Klomfass et al., 2nd Quarterly Status Report, EMI Report I-13/08.
- [2] <http://tetgen.berlios.de/>
- [3] www.geodict.com
- [4] www.simpleware.com
- [5] P. B. Bochev, C. R. Dohrmann, M. D. Gunzburger. Stabilization of low-order mixed finite elements for the Stokes equations. SIAM J. Numer. Anal. 44/1, 82–101, 2006.
- [6] E. A. de Souza Neto, F. M. Andrade Pires, D. R. J. Owen. F-bar-based linear triangles and tetrahedra for finite strain analysis of nearly incompressible solids. Part I: formulation and benchmarking. Int. J. Numer. Meth. Engng. 62, 353–383, 2005.
- [7] J. Bonet, A. J. Burton. A simple average nodal pressure tetrahedral element for incompressible and nearly incompressible dynamic explicit applications. Commun. Numer. Meth. Engng. 14, 437–449, 1998.
- [8] P. Hauret, E. Kuhl, M. Ortiz. Diamond elements: A finite element / discrete-mechanics approximation scheme with guaranteed optimal convergence in incompressible elasticity. Int. J. Numer. Meth. Engng. 72, 253–294, 2007.
- [9] J. Rojek, E. Oñate, R. L. Taylor. CBS-based stabilization in explicit solid dynamics. Int. J. Numer. Engng. 66, 1547–1568, 2006.
- [10] E. Oñate, J. Rojek, R. L. Taylor, O. C. Zienkiewicz. Finite calculus formulation for incompressible solids using linear triangles and tetrahedra. Int. J. Numer. Meth. Engng. 59, 1473–1500, 2004.
- [11] O. C. Zienkiewicz, R. L. Taylor, J. Z. Zhu. The finite element method: Its basis and fundamentals. Sixth edition, Elsevier Butterworth-Heinemann, 2005.

- [12] A. Pandolfi and M. Ortiz. An Efficient Adaptive procedure for three-dimensional fragmentation simulations. *Engineering with Computers* 18, 184–159, 2002.
- [13] M. Ortiz and A. Pandolfi. Finite-deformation irreversible cohesive elements for three-dimensional crack-propagation Analysis. *Int. J. Numer. Meth. Engng.* 44, 1267–1282, 1999.
- [14] O. Nguyen, M. Ortiz. Coarse graining and renormalization of atomistic binding relations and universal macroscopic cohesive behaviour. *Journal of the Mechanics and Physics of Solids* 50, 1727–1741, 2002.

List of Distribution

Report No. I-32/08

Copies: 8 + 2 CDs

Author: Arno Klomfass

Title: **Characterization of the Material Microstructure for Reactive Material Design – 3rd Quarterly Progress Report II/2008**

Internal Distribution:

Author(s): Bagusat, Knell, Klomfass, Linnemann, Sauer, Steinhauser

External Distribution:

Gil Graff (Technical Representative) PDF
Office of Naval Research
875 North Randolph Street
Arlington, VA 22203-1995
USA
gil.graff@navy.mil

Dr. Judah Goldwasser PDF
DARPA/DSO
3701 North Fairfax Dr
Arlington, VA 22203
USA
Judah.Goldwasser@darpa.mil

Clifford Bedford, Ph.D. PDF
Program Manager Code 351
Advanced Energetics Materials
Office of Naval Research
875 N. Randolph St.
Arlington, VA 22203-1995
Clifford.Bedford@navy.mil

Richard Ortisi 1x Hardcopy + CD
Office of Naval Research
Boston Regional Office
495 Summer St., Rm. 627
Boston, MA 02210-2109

Defense Technical Information Center 1x Hardcopy +CD
8725 John J Kingman Road Ste 0944
Fort Belvoir, VA 22060-6218

REPORT DOCUMENTATION PAGE					<i>Form Approved OMB No. 0704-0188</i>	
<p>The public reporting burden for this collection of information is estimated to average 1 hour per response, including the time for reviewing instructions, searching existing data sources, gathering and maintaining the data needed, and completing and reviewing the collection of information. Send comments regarding this burden estimate or any other aspect of this collection of information, including suggestions for reducing the burden, to Department of Defense, Washington Headquarters Services, Directorate for Information Operations and Reports (0704-0188), 1215 Jefferson Davis Highway, Suite 1204, Arlington, VA 22202-4302. Respondents should be aware that notwithstanding any other provision of law, no person shall be subject to any penalty for failing to comply with a collection of information if it does not display a currently valid OMB control number.</p> <p>PLEASE DO NOT RETURN YOUR FORM TO THE ABOVE ADDRESS.</p>						
1. REPORT DATE (DD-MM-YYYY)		2. REPORT TYPE			3. DATES COVERED (From - To)	
4. TITLE AND SUBTITLE				5a. CONTRACT NUMBER		
				5b. GRANT NUMBER		
				5c. PROGRAM ELEMENT NUMBER		
6. AUTHOR(S)				5d. PROJECT NUMBER		
				5e. TASK NUMBER		
				5f. WORK UNIT NUMBER		
7. PERFORMING ORGANIZATION NAME(S) AND ADDRESS(ES)					8. PERFORMING ORGANIZATION REPORT NUMBER	
9. SPONSORING/MONITORING AGENCY NAME(S) AND ADDRESS(ES)					10. SPONSOR/MONITOR'S ACRONYM(S)	
					11. SPONSOR/MONITOR'S REPORT NUMBER(S)	
12. DISTRIBUTION/AVAILABILITY STATEMENT						
13. SUPPLEMENTARY NOTES						
14. ABSTRACT						
15. SUBJECT TERMS						
16. SECURITY CLASSIFICATION OF:			17. LIMITATION OF ABSTRACT	18. NUMBER OF PAGES	19a. NAME OF RESPONSIBLE PERSON	
a. REPORT	b. ABSTRACT	c. THIS PAGE			19b. TELEPHONE NUMBER (Include area code)	

INSTRUCTIONS FOR COMPLETING SF 298

1. REPORT DATE. Full publication date, including day, month, if available. Must cite at least the year and be Year 2000 compliant, e.g. 30-06-1998; xx-06-1998; xx-xx-1998.

2. REPORT TYPE. State the type of report, such as final, technical, interim, memorandum, master's thesis, progress, quarterly, research, special, group study, etc.

3. DATES COVERED. Indicate the time during which the work was performed and the report was written, e.g., Jun 1997 - Jun 1998; 1-10 Jun 1996; May - Nov 1998; Nov 1998.

4. TITLE. Enter title and subtitle with volume number and part number, if applicable. On classified documents, enter the title classification in parentheses.

5a. CONTRACT NUMBER. Enter all contract numbers as they appear in the report, e.g. F33615-86-C-5169.

5b. GRANT NUMBER. Enter all grant numbers as they appear in the report, e.g. AFOSR-82-1234.

5c. PROGRAM ELEMENT NUMBER. Enter all program element numbers as they appear in the report, e.g. 61101A.

5d. PROJECT NUMBER. Enter all project numbers as they appear in the report, e.g. 1F665702D1257; ILIR.

5e. TASK NUMBER. Enter all task numbers as they appear in the report, e.g. 05; RF0330201; T4112.

5f. WORK UNIT NUMBER. Enter all work unit numbers as they appear in the report, e.g. 001; AFAPL30480105.

6. AUTHOR(S). Enter name(s) of person(s) responsible for writing the report, performing the research, or credited with the content of the report. The form of entry is the last name, first name, middle initial, and additional qualifiers separated by commas, e.g. Smith, Richard, J, Jr.

7. PERFORMING ORGANIZATION NAME(S) AND ADDRESS(ES). Self-explanatory.

8. PERFORMING ORGANIZATION REPORT NUMBER. Enter all unique alphanumeric report numbers assigned by the performing organization, e.g. BRL-1234; AFWL-TR-85-4017-Vol-21-PT-2.

9. SPONSORING/MONITORING AGENCY NAME(S) AND ADDRESS(ES). Enter the name and address of the organization(s) financially responsible for and monitoring the work.

10. SPONSOR/MONITOR'S ACRONYM(S). Enter, if available, e.g. BRL, ARDEC, NADC.

11. SPONSOR/MONITOR'S REPORT NUMBER(S). Enter report number as assigned by the sponsoring/monitoring agency, if available, e.g. BRL-TR-829; -215.

12. DISTRIBUTION/AVAILABILITY STATEMENT. Use agency-mandated availability statements to indicate the public availability or distribution limitations of the report. If additional limitations/ restrictions or special markings are indicated, follow agency authorization procedures, e.g. RD/FRD, PROPIN, ITAR, etc. Include copyright information.

13. SUPPLEMENTARY NOTES. Enter information not included elsewhere such as: prepared in cooperation with; translation of; report supersedes; old edition number, etc.

14. ABSTRACT. A brief (approximately 200 words) factual summary of the most significant information.

15. SUBJECT TERMS. Key words or phrases identifying major concepts in the report.

16. SECURITY CLASSIFICATION. Enter security classification in accordance with security classification regulations, e.g. U, C, S, etc. If this form contains classified information, stamp classification level on the top and bottom of this page.

17. LIMITATION OF ABSTRACT. This block must be completed to assign a distribution limitation to the abstract. Enter UU (Unclassified Unlimited) or SAR (Same as Report). An entry in this block is necessary if the abstract is to be limited.